Tectonophysics 910 (2025) 230831

Contents lists available at ScienceDirect

Tectonophysics

journal homepage: www.elsevier.com/locate/tecto

Wedge inelasticity and fully coupled models of dynamic rupture, ocean acoustic waves, and tsunami in the Japan Trench: The 2011 Tohoku-Oki earthquake

Shuo Ma[a,*], Yue Du[a,b]

[a] Department of Earth and Environmental Sciences, San Diego State University, San Diego, CA, USA
[b] Scripps Institution of Oceanography, University of California, San Diego, CA, USA

ARTICLE INFO

Keywords:
Dynamic rupture
Inelastic deformation
Tsunami generation
Depletion in high-frequency radiation
Tsunami early warning

ABSTRACT

Along-strike variations of sediment thickness and inelastic wedge deformation can significantly affect the variations of near-trench slip, seismic radiation, and tsunamigenesis along the Japan Trench. We present fully coupled models of dynamic rupture, ocean acoustic waves, and tsunami for the 2011 M_W 9.1 Tohoku-Oki earthquake to fully investigate the physics of tsunami generation and radiation fields, by extending a dynamic rupture model with wedge inelasticity (Ma, 2023). The fully coupled models, incorporating ocean compressibility, produce tsunami in good agreement with that from a dispersive shallow-water model, confirming the validity of both models. We show strong radiation of ocean acoustic and seismic waves caused by fast rupture velocity (~3 km/s) and large near-trench slip south of 39°N, dominated by elastic wedge response. However, north of 39°N where sediment thickens in the northern Japan Trench, the inelastic wedge deformation excites tsunami efficiently with diminishing near-trench slip (<20 m), consistent with differential bathymetry observations, but causes slow rupture velocity (~850 m/s) and significantly weaker radiation of ocean acoustic and seismic waves. Inelastic wedge deformation thus provides a self-consistent interpretation to both depletion in high-frequency radiation and large tsunami generation in the northern Japan Trench in this earthquake, which may challenge the use of ocean acoustic waves for robust tsunami early warning.

1. Introduction

A controversy about the 2011 M_W 9.1 Tohoku-Oki earthquake and tsunami arose shortly after the disasters unfolded, which centers on the physics of tsunami generation and particularly why the largest tsunami (up to 40 m) occurred >100 km north of large slip region updip from the hypocenter (e.g., Mori et al., 2011). Most slip models based on seismic and geodetic data resolved large slip updip from the hypocenter (Sun et al., 2017; Lay, 2018; Uchida and Bürgmann, 2021; and references therein), confirmed by the differential bathymetry data before and after the earthquake showing >50 m slip near the trench around 38.1°N (Fujiwara et al., 2011) and seafloor geodesy data (e.g., Sato et al., 2011; Kido et al., 2011). These slip models can explain the large tsunami inundation distances in Sendai and Ishinomaki Plains; however, had little slip north of 39°N, incapable of explaining the large tsunami generation in the northern Japan Trench (e.g., MacInnes et al., 2013).

To explain the large tsunamigenesis in the northern Japan Trench, slip models by inverting tsunami data requires near-trench slip up to 36 m north of 39°N (e.g., Satake et al., 2013; Yamazaki et al., 2018). However, the differential bathymetry data in the northern Japan Trench (Fujiwara et al., 2017, Fujiwara, 2021; Kodaira et al., 2020, 2021; Zhang et al., 2023) showed the trenchward coseismic horizontal displacement <20 m, inconsistent with these models. A large submarine landslide for tsunami generation (Tappin et al., 2014) was also considered unlikely from the differential bathymetry data (Fujiwara et al., 2017). Another important observation is that the turbidite units that are strongly correlated with large slip at trench and strong ground motion south of 38.7°N were not observed in the northern Japan Trench (e.g., Ikehara et al., 2018; Uchida and Bürgmann, 2021), indicating a different deformation mode north of 38.7°N.

Nearly all the slip models for this earthquake are based on elastic dislocation theory, which requires large shallow slip to explain tsunami generation (e.g., Satake and Tanioka, 1999; Lay et al., 2012). Despite being inconsistent with the differential bathymetry data and turbidite

---

* Corresponding author.
E-mail address: sma@sdsu.edu (S. Ma).

https://doi.org/10.1016/j.tecto.2025.230831
Received 23 March 2025; Received in revised form 12 June 2025; Accepted 17 June 2025

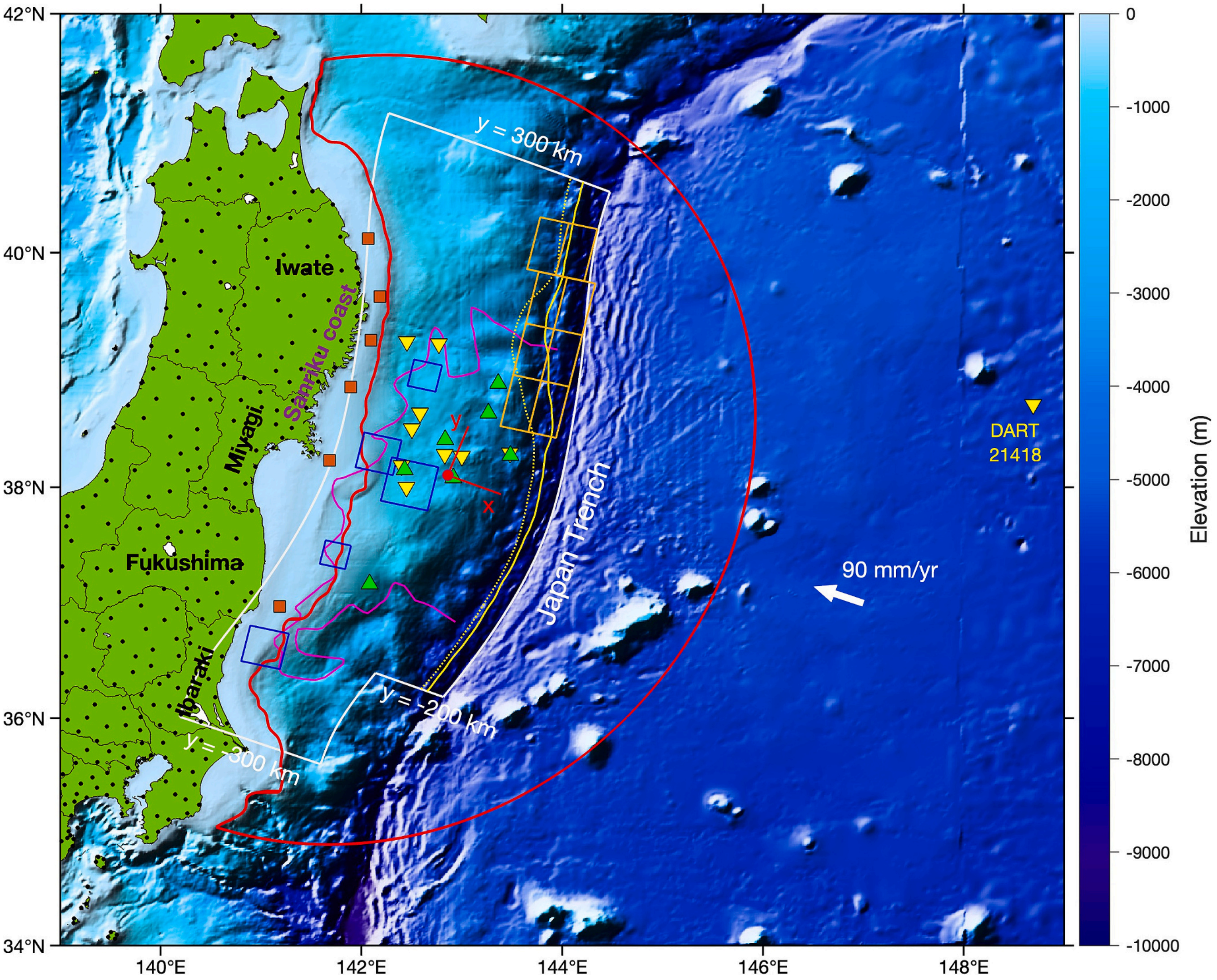

Fig. 1. Map of the study. The fault surface used in this work is outlined by white. The red dot denotes the epicenter of the 2011 Tohoku-Oki earthquake, which is the origin of the coordinate system used (shown in red, *x* axis is along the plate convergence direction). The magenta curve shows the coseismic rupture area inferred by Kato and Igarashi (2012). The blue squares are the strong motion generation areas (SMGAs) identified by Kurahashi and Irikura (2013). The yellow solid and dotted lines denote the traces of the backstop surface on the seafloor and plate interface, respectively, by fitting the sediment-thickness data of Tsuru et al. (2002). Thicker sediments in the northern Japan Trench can be clearly seen. The 8 subfaults of Satake et al. (2013, 2017) in the northern Japan Trench depict the rupture zone of the 1896 Sanriku earthquake. Stations shown are on-land GPS stations (black dots), GPS buoys (orange squares), OBP sensors (yellow inverted triangles), and off-shore GPS stations (green triangles). The four prefectures mentioned in the paper and the Sanriku coast are denoted. These features are identical to those in Fig. 1 of Ma (2023). The red crescent-shaped curve is the boundary of the ocean of interest considered in this work; the irregular western boundary coincides approximately with the 400 m-depth bathymetry contour. (For interpretation of the references to colour in this figure legend, the reader is referred to the web version of this article.)

observations in the northern Japan Trench large shallow slip is still the prevailing hypothesis in explaining the 2011Tohoku tsunami and large tsunami runup north of 39°N and has been widely used to explain tsunamigenesis around the globe (e.g., Cheung et al., 2021).

A different and opposing hypothesis was proposed by Ma and Nie (2019) and Ma (2023), which resorts to inelastic wedge deformation (Ma, 2012; Ma and Hirakawa, 2013). They questioned the application of the elastic dislocation theory in the northern Japan Trench, where weak and thick sediments are present in the frontal prism (Tsuru et al., 2002; Kodaira et al., 2017). Fig. 1 shows the variation of sediment thickness along the Japan Trench based on the data of Tsuru et al. (2002). With weak sediments large dynamic stresses during rupture propagation can drive the wedge into failure, making the elastic dislocation theory less applicable. We refer the reader to Ma and Nie (2019), Wilson and Ma (2021), Du et al. (2021), and Ma (2023) for more discussions of the applicability of elastic dislocation theory in shallow subduction zones. Inelastic deformation of overriding wedge, mimicking frictional sliding on Coulomb microfractures with steeper dips, can efficiently generate seafloor uplift on a shallowly dipping plate interface with diminishing shallow slip. Ma (2023) showed that the along-strike variation of sediment thickness and inelastic deformation in the northern Japan Trench can explain the large shallow near-trench slip (>50 m) around 38.1°N and large tsunami generation with diminishing shallow slip (< 20 m) north of 39°N, providing a self-consistent explanation to the puzzling >100 km distance offset mentioned above while being consistent with the differential bathymetry observations (Fujiwara et al., 2011, 2017, Fujiwara, 2021; Kodaira et al., 2020, 2021). The inelastic deformation of the model produces short-wavelength uplift, generating impulsive tsunami that matches the amplitude, arrival time, and pulse width of the tsunami observed offshore the Sanriku coast (e.g., Maeda et al., 2011). The impulsive tsunami has been shown to be instrumental in leading to extreme runup in the rugged Sanriku coast due to amplification of short-wavelength components (e.g., Shimozono et al., 2014; Tappin et al., 2014; Yamazaki et al., 2018; Du et al., 2021).

It is important to further test these two hypotheses, as the seemingly puzzling observations may illuminate the physics of tsunami generation. One way to do so is to examine the radiation characteristics of elastic dislocation models and models with significant inelastic wedge deformation (e.g., Wilson and Ma, 2021). Since Kanamori (1972) identified tsunami earthquakes as earthquakes that generate disproportionately large tsunamis relative to their surface wave magnitude (M_S) depletion in high-frequency radiation had been recognized as one of the essential characteristics of tsunami earthquakes. Over the last 50 years, depletion in high-frequency radiation is also recognized as an important rupture characteristic in the upper ~10–15 km of rupture zone in large tsunamigenic earthquakes worldwide (e.g., Lay et al., 2012; Yao et al., 2013; Ye et al., 2016). Some related and important characteristics of earthquakes associated with large tsunamigenesis include anomalously slow rupture speed, long rupture duration, and low moment-scaled radiated energy (Newman and Okal, 1998). Lay et al. (2012) classified the upper 10–15 km as Domain A for global subduction zones, a domain associated with anomalously large tsunami generation and depletion in high-frequency radiation. (They associated Domain A with large slip, which may be questionable because large tsunami can be generated with diminishing slip as observed in the northern Japan Trench.)

Yet, depletion in high-frequency radiation is not well understood and largely unaccounted for in most kinematic and dynamic rupture models of large tsunamigenic earthquakes. Most models focused only on tsunami generation by shallow slip in the realm of elastic dislocation theory. Perhaps it is not surprising that slip models using seismic data failed to detect slip north of 39°N (e.g., Lay, 2018; Uchida and Bürgmann, 2021) because of the anomalous depletion in high-frequency radiation associated with large tsunami generation. The lower seismic intensity observed in Iwate Prefecture than Miyagi and Fukushima Prefectures to the south (locations shown in Fig. 1), illustrated in Fig. 1 of Kodaira et al. (2021), is also consistent with depletion in high-frequency radiation in the north. The 1896 Sanriku earthquake, one of the most anomalous tsunami earthquakes (Kanamori, 1972), also occurred in the northern Japan Trench, which strongly suggests that the same physics may lead to large tsunami generation and depletion in high-frequency radiation in both earthquakes.

How do we understand large tsunami generation and depletion in high-frequency radiation in shallow subduction zones as a whole? Noda and Lapusta (2013) argued that thermal pressurization of pore fluids in the fault zone can weaken the fault, leading to large slip and long slip duration, which can be applied to the 2011 Tohoku-Oki earthquake and 1999 Chi-Chi earthquake. However, their model was in a whole space. The rapid stress drop in their model seems unable to explain the long-duration ground velocity data as observed in the 1999 Chi-Chi earthquake. Kubota et al. (2022) showed that tsunami data is inconsistent with the possibility of thermal pressurization updip from the hypocenter; large shallow slip is driven mostly by deep large stress drop enhanced by the free surface. Ma and Hirakawa (2013) showed the importance of the free surface in enhancing depletion in high-frequency radiation as it unclamps the fault and causes large but more gradual strength drop than deep rupture. Yin and Denolle (2021) showed similar results. However, the free surface alone may not account for the full physics for depletion in high-frequency radiation. Meng and Duan (2023) suggested that along-strike frictional heterogeneities (Bilek and Lay, 2002) may lead to slow rupture propagation, depletion in high-frequency radiation, and low moment-scaled radiated energy, but the radiation from their model may need to be further examined because locally large stress drops on velocity-weakening fault patches (similar to the seamount rupture modelled by Duan, 2012) may enhance high-frequency radiation. All these models are elastic (except for Ma and Hirakawa, 2013) and require large shallow slip to explain tsunami generation.

Many early studies (e.g., Okal, 1988; Kanamori and Kikuchi, 1993; Satake and Tanioka, 1999; Polet and Kanamori, 2000) attributed anomalous depletion in high-frequency radiation and tsunamigenesis to sediment at shallow depth or in the fault zone based on somewhat oversimplified physics, discussed by Ma (2023). A recent study can be seen in Sallarès and Ranero (2019). These studies argued that if seismic moment is fixed the low rigidity of sediment increases slip, therefore increasing seafloor displacement and tsunami generation. To explain depletion in high-frequency radiation most studies attributed to slow rupture velocity, again due to low rigidity of sediment. However, in a low-velocity fault zone rupture velocity is not fully controlled by the sediment in all conditions, instead it can be controlled by the material outside the fault zone. Trapped waves within the low-velocity fault zone can lead to more high-frequency radiation and sometime to supershear rupture velocities (Harris and Day, 1997). Lotto et al. (2017) modelled dynamic rupture propagation in the presence of a large sedimentary prism and found that sediment leads to slow rupture propagation and large slip, similar to the elastic models in Ma (2023) and this work. However, dynamic rupture on a bimaterial interface may lead to large and rapid strength drop enhanced by the free surface (Ma and Beroza, 2008; Scholz, 2014), again contributing to high-frequency radiation.

One mechanism that appear to reconcile probably all the anomalous observations of shallow subduction earthquakes is inelastic deformation (Ma, 2012; Ma and Hirakawa, 2013). Seno (2000) and Tanioka and Seno (2001a, 2001b) first proposed the concept of inelastic deformation and showed that inelastic deformation can generate tsunami efficiently with slip smaller than required in elastic dislocation models. Their model was conceptual without including realistic constitutive modelling of inelastic deformation. Neither did they relate inelastic deformation to anomalous rupture characteristics (recent examples can be seen in Gusman et al., 2012 and Hill et al., 2012). Ma (2012) modelled inelastic wedge deformation using undrained Mohr-Coulomb yield criterion and showed that inelastic deformation can lead to slow rupture velocity and efficient tsunamigenesis with reduced slip. Ma and Hirakawa (2013) further showed that inelastic deformation is a large energy sink, which can explain depletion in high-frequency radiation and low moment-scaled radiated energy for shallow subduction earthquakes. The free surface also exerts a fundamental control on inelastic deformation because the yielding of Coulomb materials is depth-dependent, leading to flower-like damage zones in a strike-slip setting (e.g., Ma, 2008; Ma and Andrews, 2010; Ma, 2022). Ma and Nie (2019) extended the inelastic deformation model to 3D and proposed the concept that along-strike variations of sediment thickness and inelastic wedge deformation can explain the puzzling large tsunami generation more than 100 km north of the epicenter in the 2011 Tohoku tsunami. In Ma (2023), the dynamic rupture model with inelastic deformation in the northern Japan Trench for the 2011 Tohoku-Oki earthquake reduces the along-strike rupture velocity to ~850 m/s, which explains the timing of tsunami off the Sanriku coast, in contrast to the 3-min delay of shallow slip required by the elastic dislocation model of Satake et al. (2013). These results show that sediment can play a critical role in tsunami generation and deficiency in high-frequency radiation in its weak strength leading to inelastic deformation, rather than low rigidity identified in previous studies.

Here we present fully coupled models of dynamic rupture, ocean acoustic waves, and tsunami for the 2011 Tohoku-Oki earthquake, focusing on tsunami generation and different radiation characteristics of seismic and acoustic waves based on elastic and inelastic models of Ma (2023). Fully coupled models allow rigorous simulation of tsunami generation and propagation as well as ocean acoustic and seismic waves (e.g., Lotto and Dunham, 2015; Lotto et al., 2018; Wilson and Ma, 2021; Ma, 2022; Abrahams et al., 2023; Kutschera et al., 2024). We will show that inelastic wedge deformation in the northern Japan Trench leads to more depletion of high-frequency radiation than models with elastic deformation while generating tsunami more efficiently. The results will shed new light on the validity of different hypotheses in explaining the devastating 2011 Tohoku tsunami and have important implications for tsunami hazard assessments and reductions worldwide. Because ocean acoustic waves travel faster than tsunami there were studies advocating

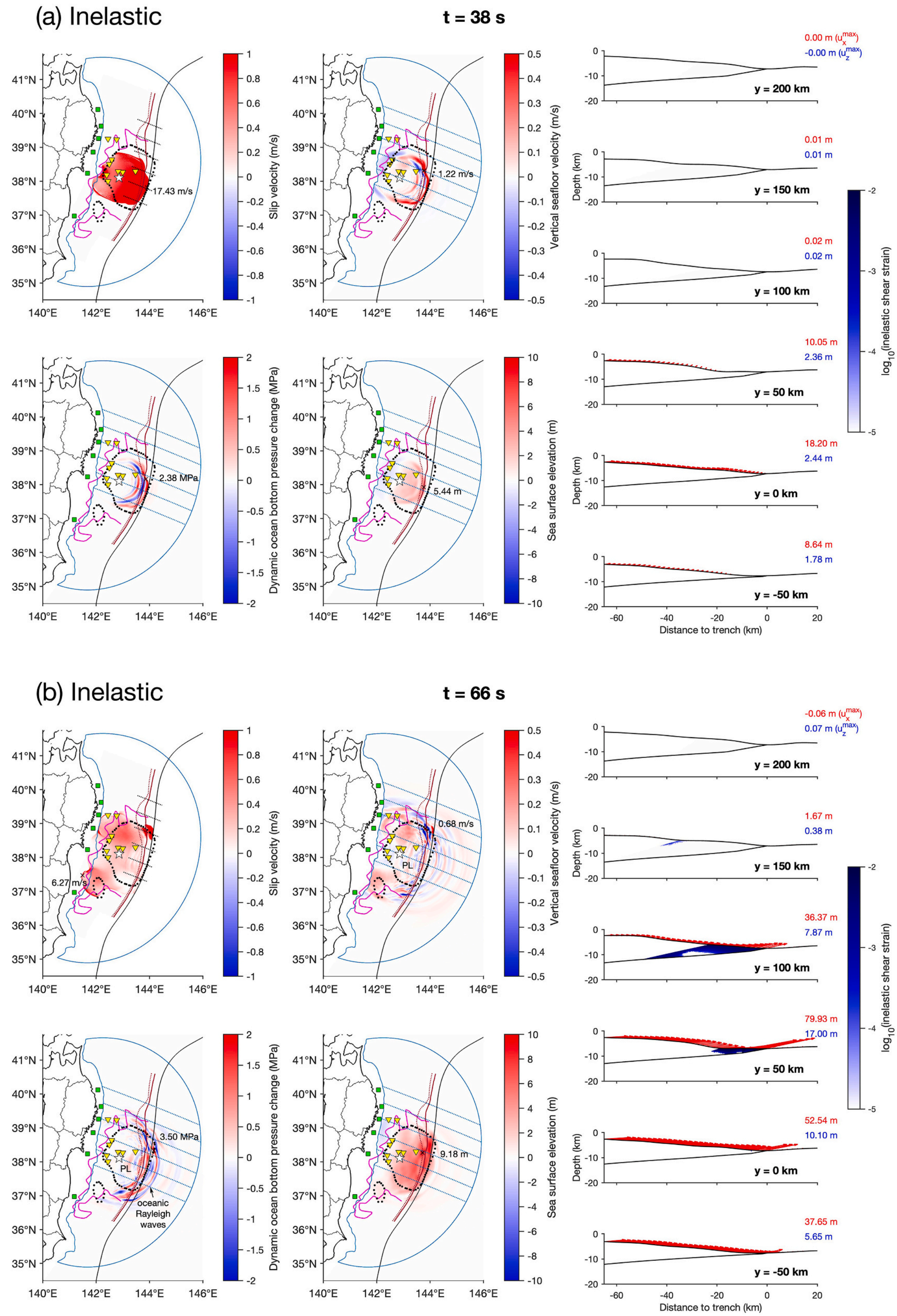

Fig. 2. Snapshots of slip velocity, vertical seafloor velocity, dynamic ocean bottom pressure change, sea surface elevation, and seafloor displacements at 6 cross sections (marked by thin black dotted lines) are shown for the inelastic (a – c) and elastic (d) models. The peak amplitude and location (denoted by a symbol ×) are shown in each panel. The inelastic strain in the wedge is also shown in (a – c). The thick black dotted line shows the 15 m contours of slip model of Iinuma et al. (2012). The fully coupled models capture both ocean acoustic and seismic waves and tsunami. Wave fields are complex. Different radiations and seafloor displacements in the northern Japan Trench due to different rupture characteristics between the two models at 124 s are seen with significantly weaker radiation in the inelastic model. PL and oceanic Rayleigh waves are marked. More details about the two models are illustrated in Movies 1 and 2.

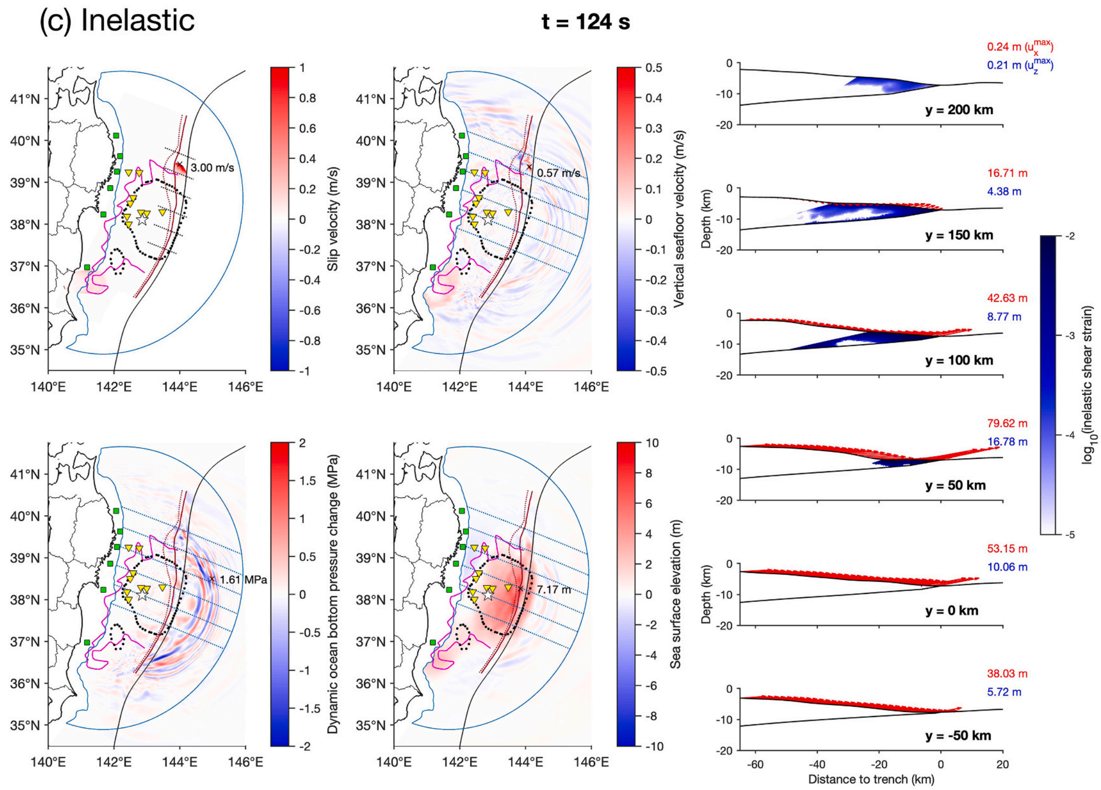

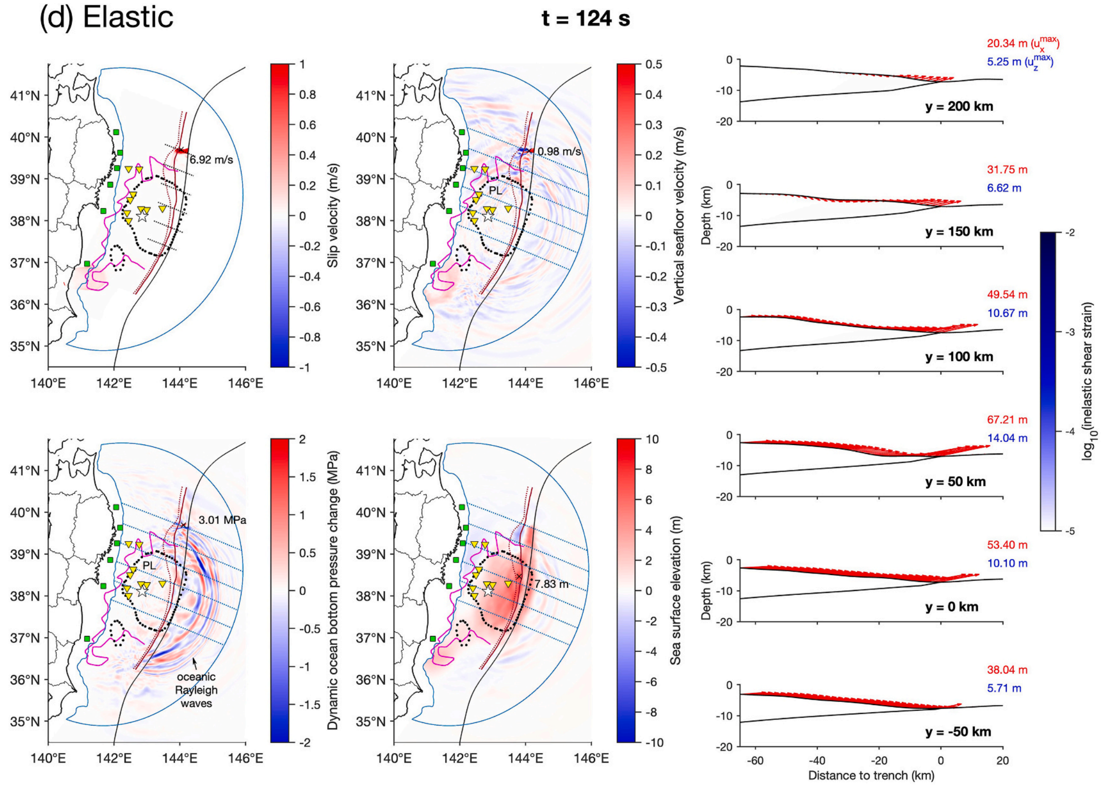

Fig. 2. (*continued*).

ocean acoustic waves for tsunami early warning (e.g., Ewing et al., 1950; Kozdon and Dunham, 2014; Mei and Kadri, 2017; Lay et al., 2019; Gomez and Kadri, 2023). However, depletion in high-frequency radiation may pose a challenge to use ocean acoustic waves for robust tsunami early warning because the periods of these waves are significantly shorter than that of tsunami and they can be strongly weakened by inelastic deformation.

We will also show that moderate inelastic deformation coupled with ocean response can significantly increase slip duration, leading to locally large shallow slip >100 m south of 39°N (in contrast to diminishing shallow slip with intense inelastic deformation in the northern Japan Trench), which may be observed in Ueda et al. (2023). Such locally large shallow slip, however, may not contribute much to tsunami generation because of small wavelength of seafloor uplift compared to ocean depth. Increase of slip duration by inelastic deformation may explain the long-period ground motion recorded in the northern rupture zone of the 1999 Chi-Chi earthquake (Ma et al., 2003), which will be addressed in a separate study.

2. Fully coupled models

Our fully coupled models of dynamic rupture, ocean acoustic wave, and tsunami for the 2011 Tohoku-Oki earthquake are directly based on the dynamic rupture models of Ma (2023), which presented two models: one elastic model and one model with inelastic wedge deformation (mostly in the northern Japan Trench). Both models were based on a heterogeneous stress drop model of Kubota et al. (2022), constrained by on- and off-shore GPS and tsunami data. The fault geometry, bathymetry, and velocity structure were based on the Japan Integrated Velocity Structure Model (JIVSM) of Koketsu et al. (2012). The results from both models are nearly identical due to the same model setup except in the northern Japan Trench, where the elastic model showed large slip (>40 m) at the trench, fast rupture velocity, and large slip velocity, while the inelastic model showed diminished slip (<20 m) at the trench, slow rupture velocity (~850 m/s), and small slip velocity due to sediment yielding. The large shallow slip in the elastic model violates the differential bathymetry observations north of 39°N (Fujiwara et al., 2017) and produces tsunami larger and earlier than the observations offshore the Sanriku coast. In contrast, the inelastic model is consistent with the differential bathymetry and tsunami observations. These different rupture characteristics between the two models will also be seen in the fully coupled models below.

Fig. 1 shows the map of this study, depicting the bathymetry, fault geometry, sedimentary wedge with along-strike variation of sediment thickness (Tsuru et al., 2002), strong motion generation areas (SMGAs, Kurahashi and Irikura, 2013), and geodetic and tsunami stations considered in Ma (2023). The coordinate system used in this work is identical to the one in Ma (2023): the x axis is along the plate convergence direction (E20°S), y axis along N20°E, z axis vertical up, and the origin located at the epicenter (38°06.2′ N, 142°51.6′E). The fault extends 200 km wide (along x) and 600 km long (along y), which reaches the trench at -200 km $\leq y \leq 300$ km and is buried at $y \leq -200$ km.

The reader is referred to Ma (2023) for the detailed set up of the models, which remains identical in this work. The only minor difference is in the inelastic model here where the wedge slope and fault dip are fit by using only the sediment part of the wedge, i.e., seaward from backstop (Fig. S1), which give rise to 5.4149° (wedge slope) and 4.5571° (fault dip). Ma (2023) obtained slightly different parameters by fitting the data within 65 km from the trench to consider possible inelastic deformation in the inner wedge. We allow inelastic deformation only in the sediment seaward from backstop in this work. These parameters set the stresses and strength parameters in the wedge; however, the results only show slight differences from Ma (2023) as will be shown below.

To fully couple dynamic rupture, ocean acoustic waves, and tsunami, we add a compressible ocean to the models of Ma (2023). To create the ocean in the model, we first create a hemiellipsoid (three axes are 340, 380, and 340 km along the three coordinate axes) centered at (−80 km, −10 km, 0) to intersect the ocean and seafloor. We then make a horizontal cut at 400 m depth on the seafloor near the coast (the bathymetry is slightly smoothed so that the 400 m contour is a single curve) and slice the 400 m contour up along an inclination angle 15° to intersect the sea surface, which creates a small irregular dipping surface that becomes the western boundary of the ocean. The hemiellipsoid and seafloor (with realistic bathymetry) form the remaining boundary of the ocean of interest in the model (Fig. 1). We use 4-node tetrahedral elements (element size ~500 m) to mesh the ocean. The period of the fundamental mode of ocean acoustic waves is approximately $4H/c$ (H is ocean depth and c is the sound speed in the ocean), which is 16 s for an ocean depth 6 km. The element size 500 m can simulate accurately the propagation of ~3 s ocean acoustic waves for 10 elements per minimum wavelength, which can well resolve the propagation of the fundamental mode of ocean acoustic waves in ocean depths >1.25 km. To minimize wave reflections at ocean-solid boundaries, we further extend the ocean outward for an additional ~300 km with a coarser mesh (not shown).

The coupling between the ocean and solid earth at the seafloor is done by enforcing continuity of normal displacement and traction and vanishing shear traction. To include gravity waves in the model we use a linearized sea surface boundary condition of Lotto and Dunham (2015), verified by a semi-analytical solution in Wilson and Ma (2021). This free surface boundary condition naturally gives rise to dispersions of ocean acoustic waves and tsunami in the linear regime. The fully coupled models account for generation and propagation of gravity waves in the ocean, including the contributions of horizontal displacement of sloping seafloor and rupture duration on tsunami generation as well as filtering of short-wavelength uplift features by variable ocean depth (e.g., Lotto et al., 2018; Wilson and Ma, 2021), which may be the most accurate method in modelling tsunami although the computational expense is high compared to the widely-used shallow water models, thoroughly discussed by Abrahams et al. (2023). The feedback of ocean on the solid earth is also rigorously simulated. We refer the reader to these papers for the detailed descriptions of the fully coupled modelling approach. A special treatment is done at trench in the models here because 3 nodes coincide at each point in the finite element mesh; we use the velocity and displacement of the center of mass of hanging wall and footwall nodes to interact with the ocean node in enforcing the boundary conditions at seafloor. We run the models for 500 s with a time step of 0.01 s.

3. Results

To illustrate the fully coupled models, we show 3 snapshots of slip velocity, vertical seafloor velocity, dynamic ocean bottom pressure (OBP) change, sea surface elevation, and seafloor displacements and inelastic shear strain at 6 cross sections for the inelastic model (Fig. 2). In comparison, we also show one snapshot for the elastic model, which shows significantly different rupture and radiation characteristics in the northern Japan Trench. The detailed processes for these two fully coupled models are illustrated in Movies 1 and 2. The rupture processes with ocean are nearly identical to the results of Ma (2023) without ocean except for some differences at shallow depths (to be shown below), as in general the ocean has a minor effect on the response of solid earth (e.g., Lotto et al., 2018).

Shortly after nucleation, the rupture expands in all directions driven by the large stress drop (~10 MPa) around the hypocenter. The rupture propagates faster up dip (mode II direction) with a rupture velocity ~ 3 km/s. Significant along-strike propagation at depth is also seen due to large stress drop along strike (see also Fig. 7b of Ma, 2023), although the rupture velocity is slower along the mode III direction. Strong seismic waves are excited, which causes rapid motion of the seafloor. The vertical seafloor velocity pattern strongly resembles the P-SV wave radiation pattern: up-dip rupture pushes the seafloor up, down-dip rupture pulls the seafloor down and the along-strike direction is a node. The up-dip rupture propagation enhanced by the free surface leads to strong directivity with large fault-normal motion, displacing seafloor mostly vertically above a shallowly dipping plate interface. Strong SH and Love waves are also excited and propagate along strike, but do not show up in vertical seafloor velocity and ocean bottom pressure. The vertical motion of seafloor compresses the ocean, generating strong P-wave in the ocean propagating upward, reflecting at sea surface and propagating downward as a pulling motion because sea surface boundary is nearly free. The reflected P-wave amplitude reverses again due to a large impedance contrast at seafloor, which gives rise to the alternating red and blue colors in vertical seafloor velocity and ocean bottom pressure

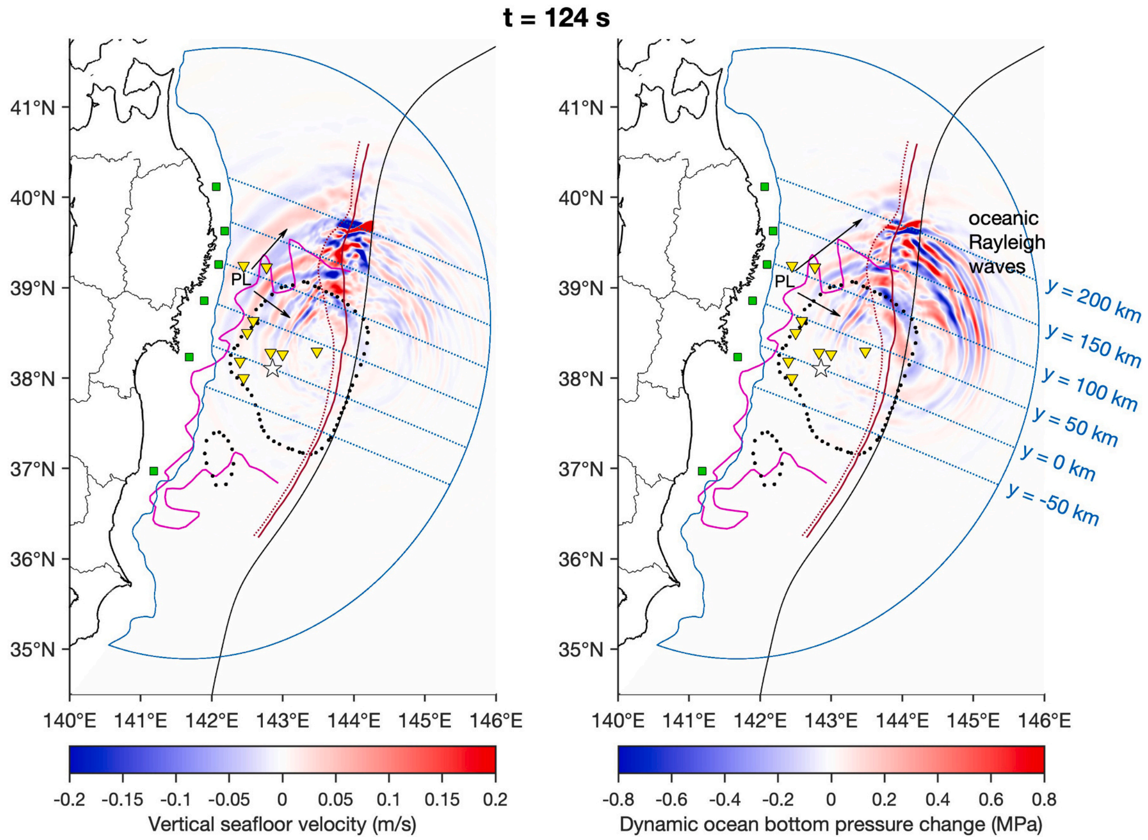

Fig. 3. Differences in vertical seafloor velocity and dynamic ocean bottom pressure change between the elastic and inelastic models at 124 s are shown. The wave fields are cleaner due to the cancellation of the same waves from earlier rupture governed by the same elastic off-fault response in both models. Due to weak radiation in the inelastic model the differences shown are mostly due to stronger radiation in the elastic model, showing clearly dispersive PL and oceanic Rayleigh waves emanating from rupture front. Strong trapped energy in the sediment behind rupture front in the elastic model is seen. (For interpretation of the references to colour in this figure legend, the reader is referred to the web version of this article.)

change as P waves bounce multiply in the ocean. The tsunami can also be seen in the sea surface elevation in the model, which has much longer wavelengths than those of the ocean acoustic waves. A cross-sectional view of these fields was clearly illustrated in the movies of 2D models of Kozdon and Dunham (2014).

As the up-dip rupture breaks the trench at ~38 s, the slip velocity reaches ~17 m/s, which generates strong radiation of different waves. The largest wave propagating seaward is oceanic Rayleigh wave. The strong reflected wave propagating landward is the PL wave (Kozdon and Dunham, 2014; Wilson and Ma, 2021), which is a leaky P wave mode due to interference of P waves trapped in the ocean and upper solid earth but is leaking energy due to conversion to S wave (e.g., Oliver and Major, 1959; Phinney, 1961). Kozdon and Dunham (2014) found a good correlation of PL wave amplitude with slip at trench. Lay et al. (2019) presented a similar concept but looked at P wave coda at teleseismic distances. Because PL waves travel much faster than that of tsunami they advocated the use of these waves for tsunami early warning. Indeed, the PL waves are strongly excited in our 3D simulations. As the rupture propagates bilaterally along strike (see 66 s), large PL wave radiation can be seen to follow behind the rupture front although the inelastic deformation has occurred (but small). However, as the rupture enters the northern Japan Trench significant inelastic wedge deformation causes slow rupture velocity (~850 m/s), small slip velocity, diminishing shallow slip, and radiation of all acoustic waves become much weaker (Fig. 2c). Large inelastic uplift occurs with diminishing horizontal displacement. In contrast, in the elastic model large acoustic radiation is clearly seen trailing behind the rupture front with large slip velocities and fast rupture velocity (Fig. 2d). Large seafloor uplift is caused by fast slip peaking at trench. In both models, rupture directivity greatly enhances the amplitudes of oceanic Rayleigh waves: they are smallest directly updip from the hypocenter but are much larger to the north and south, shown more clearly in dynamic ocean bottom pressure changes. At 124 s, the tsunami splitting above the trench can be seen.

The wavefields are complex because radiation from the rupture front is contaminated by the waves radiated from earlier rupture propagation, including breaking of the SMGAs at depth. To show the differences of radiations at rupture front between the two models we calculate the difference between the wavefields of the two models (Fig. 3). The waves due to the earlier rupture at depth are cancelled because they are identical in the two models. What remains is the difference due to radiation near trench influenced by inelastic wedge deformation. Because the radiation from inelastic deformation is much weaker the difference shown reflects largely the stronger radiation from the rupture front in the elastic model. Significant energy is trapped within the sediment behind the rupture front, which is the source of radiation. The PL waves clearly radiate from behind the rupture front but travel faster than the rupture. Some PL waves radiated from earlier rupture even arrive ahead of rupture front. The alternating blue and red colors indicate oscillatory nature of P waves trapped in the ocean. These waves are clearly dispersive; longer-wavelength components travel faster. A small, short-wavelength PL wave is seen to radiate from the trapped energy behind the rupture front and propagates slowest. The radiation of oceanic

(a) Fully coupled model

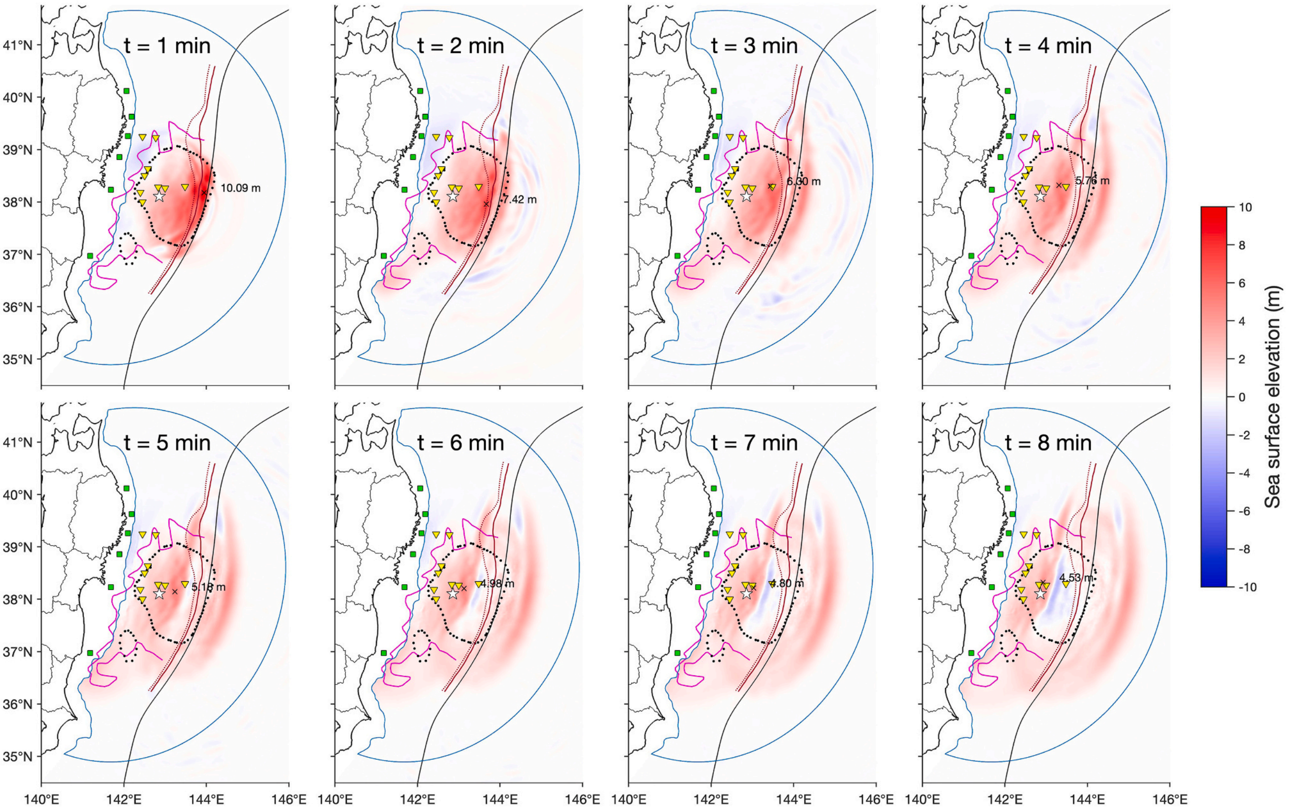

(b) Shallow water model

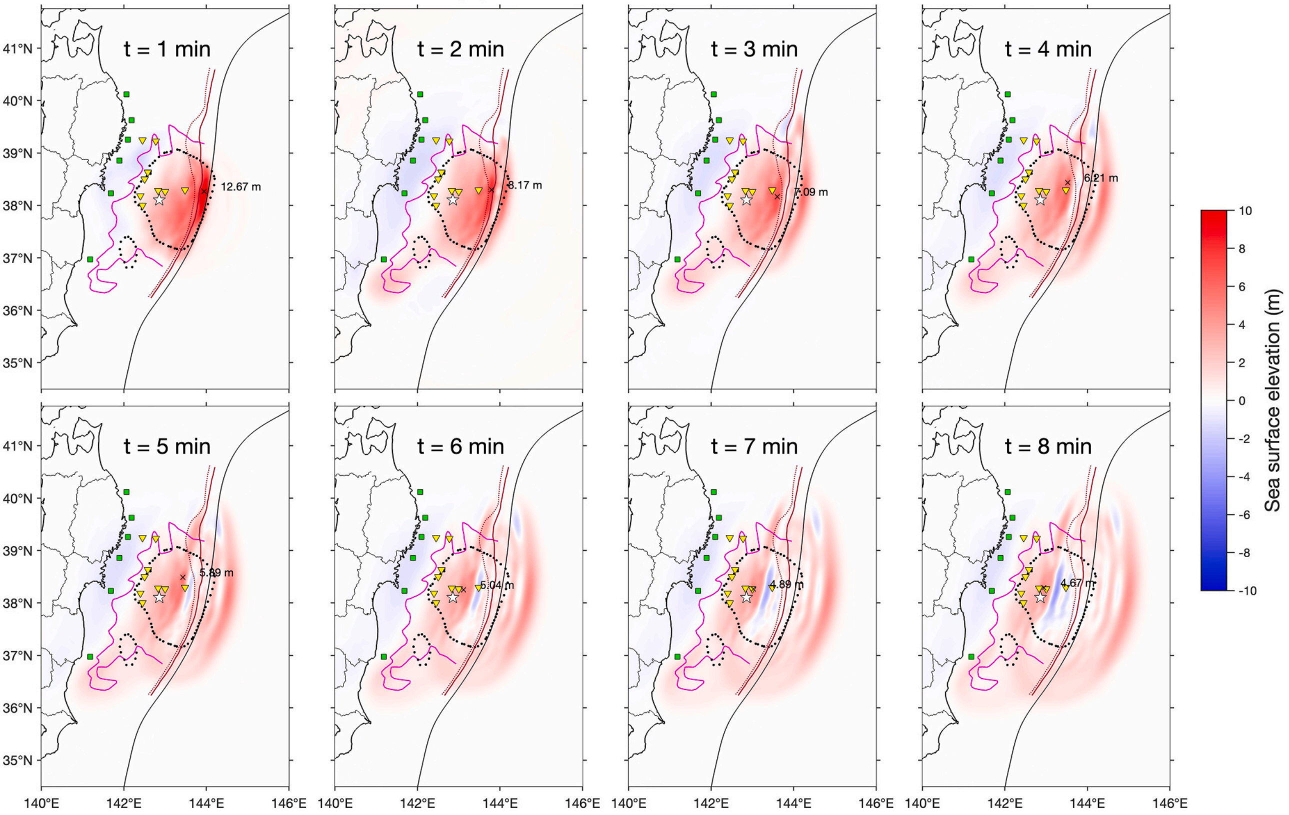

Fig. 4. Comparison of tsunamis from between the fully coupled inelastic model and shallow water model of Ma (2023) showing good agreement. (For interpretation of the references to colour in this figure legend, the reader is referred to the web version of this article.)

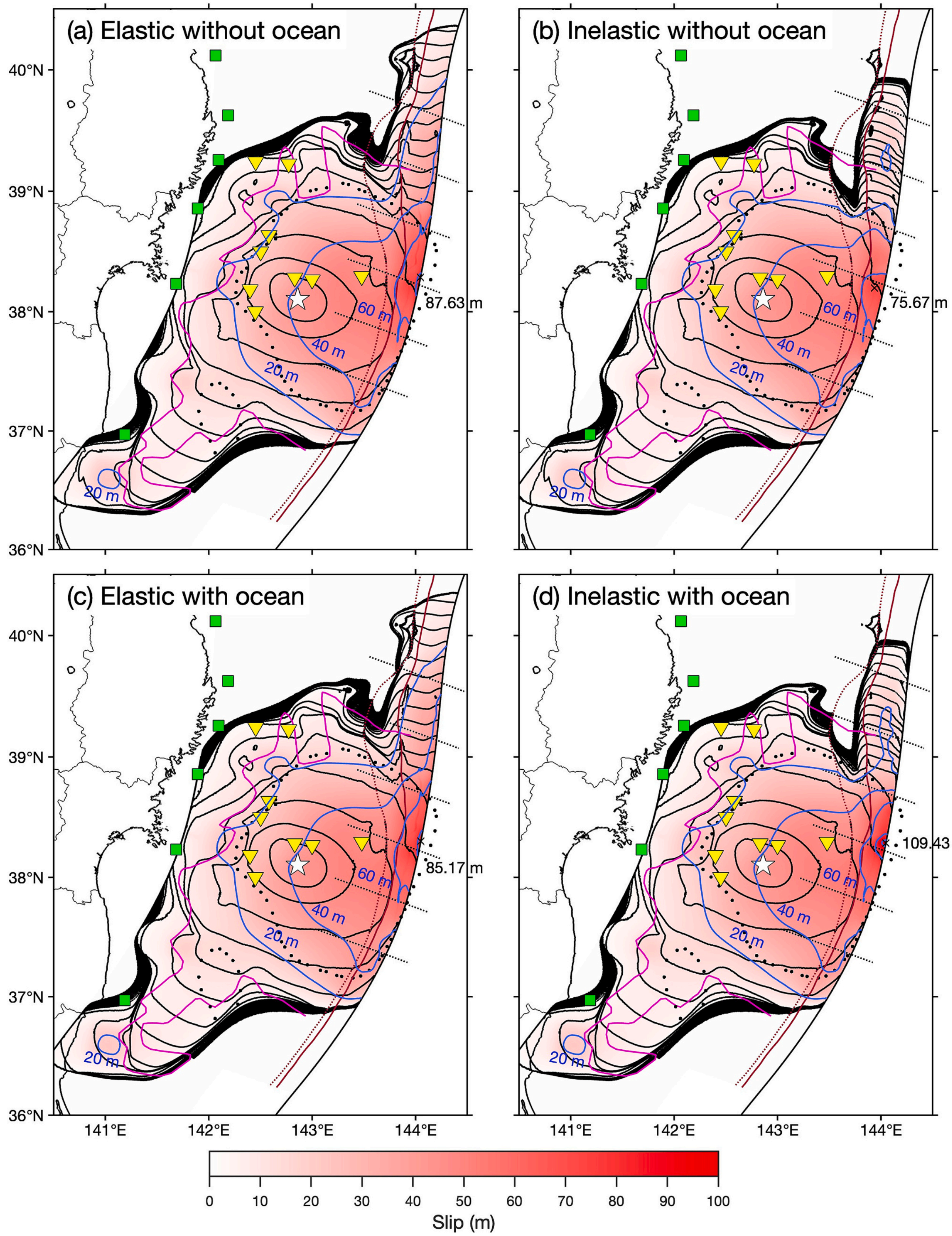

Fig. 5. Slip distributions for the elastic and inelastic models with and without ocean are shown. Black contours show rupture time every 10 s and blue contours are slip every 20 m. Slow rupture velocity (~850 m/s, indicated by the rupture time contours) and diminishing shallow slip in the northern Japan Trench are clearly seen in the two inelastic models (b, d), while elastic models (a, c) show fast rupture velocity and large shallow slip. Peak slip value is marked, and the location indicated by a symbol × . A small patch with slip >100 m is seen in (d). (For interpretation of the references to colour in this figure legend, the reader is referred to the web version of this article.)

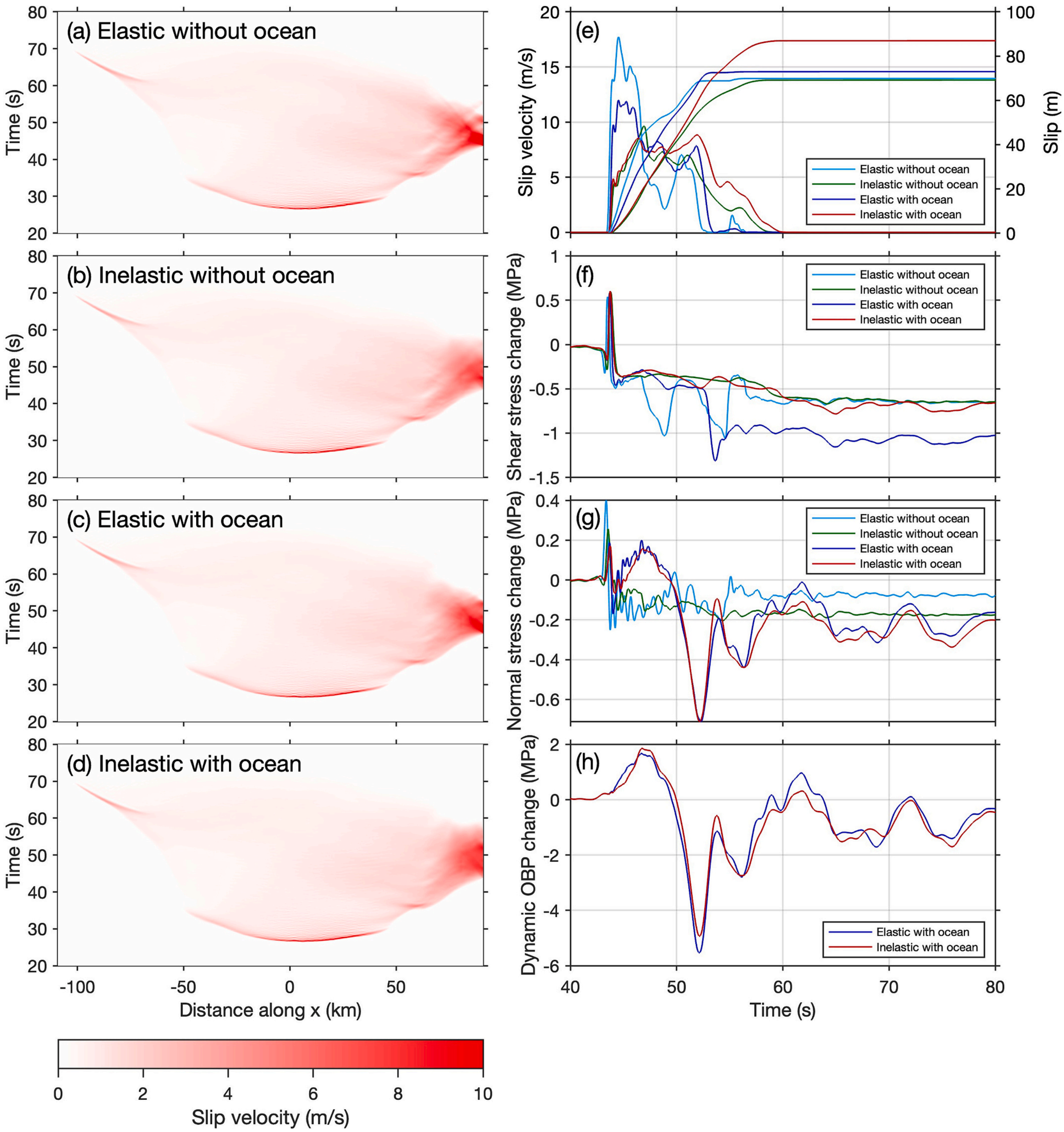

Fig. 6. Space-time plots of slip velocity at $y = 50$ km (a – d) and time histories at trench (e – h) are shown for the four models. Longer slip duration near the trench in the inelastic models can be seen in (a – d) and slip velocity time histories in (e) due to yielding and more gradual stress changes (f). Large dilation around 50 s due to P waves reflected from sea surface causes fault normal stress reduction shown in (g, h), which leads to large slip velocity increase and longer slip duration in (e). The peak slip rate is only reduced slightly by modest inelastic deformation in the model with ocean, so the long duration leads to large slip. The large shear stress reduction for the two elastic models (cyan and blue curves) around 50 s in (f) are due to decrease of slip velocity; in the rate-and-state friction as the state variable nears steady state the shear stress is proportional to the logarithm of slip velocity. (For interpretation of the references to colour in this figure legend, the reader is referred to the web version of this article.)

Rayleigh wave is also greatly reduced by inelastic wedge deformation. Clear slower propagation of oceanic Rayleigh waves than PL waves is shown as they both radiate from the rupture front. The radiation differences between elastic and inelastic models as rupture propagates are more clearly illustrated in Movies 1 and 2.

Fig. 4a shows the snapshots of tsunami from the fully coupled model with inelastic deformation, which is remarkably similar to the tsunami from a shallow water model of Ma (2023), shown in Fig. 4b. The shallow water model, assuming incompressible ocean, solved a 2D nonlinear Boussinesq equation using the time-dependent seafloor displacement

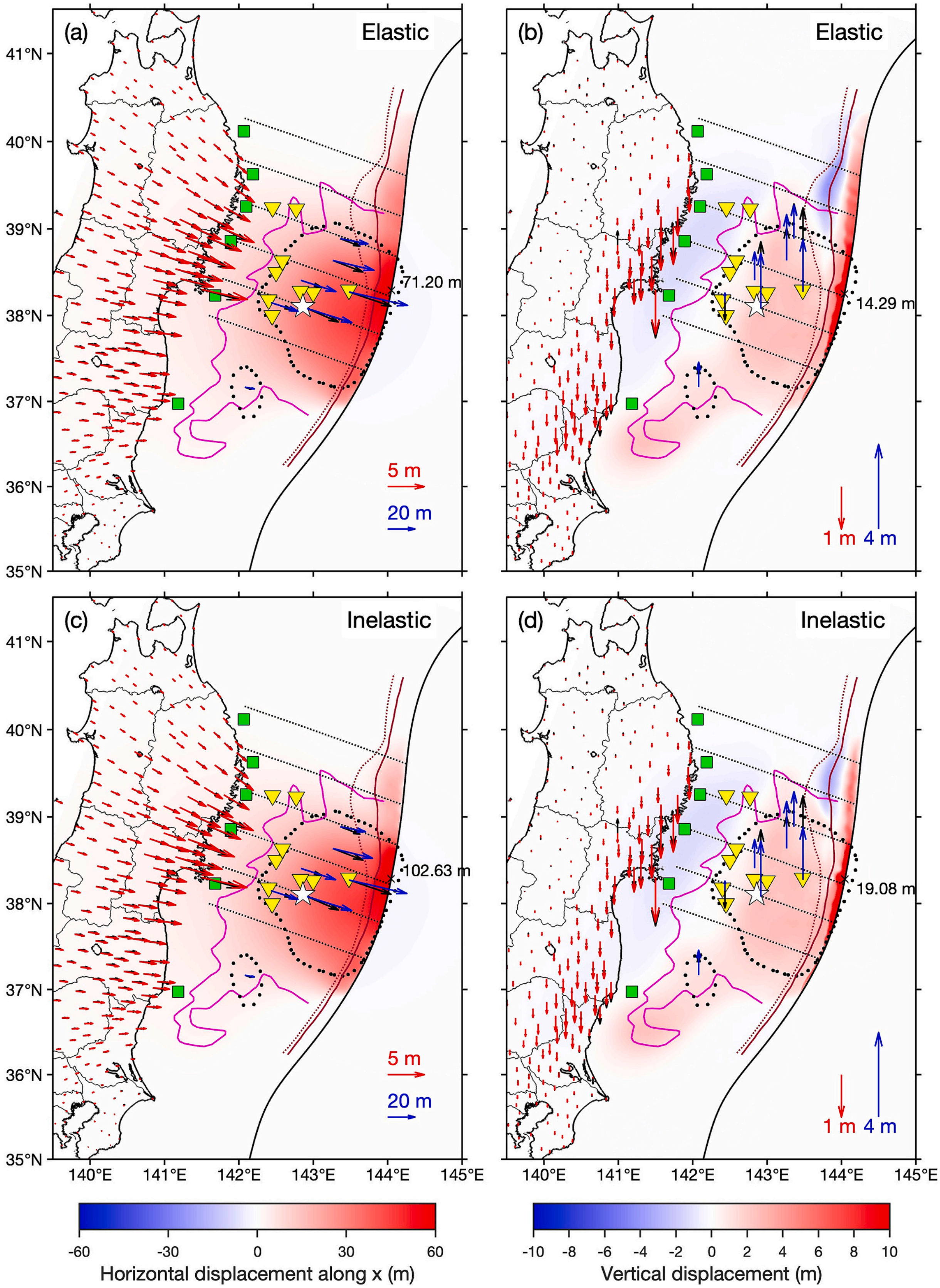

Fig. 7. Horizontal and vertical seafloor displacements from the elastic and inelastic models are compared with geodetical observations, showing little resolution of data to near-trench deformation. (For interpretation of the references to colour in this figure legend, the reader is referred to the web version of this article.)

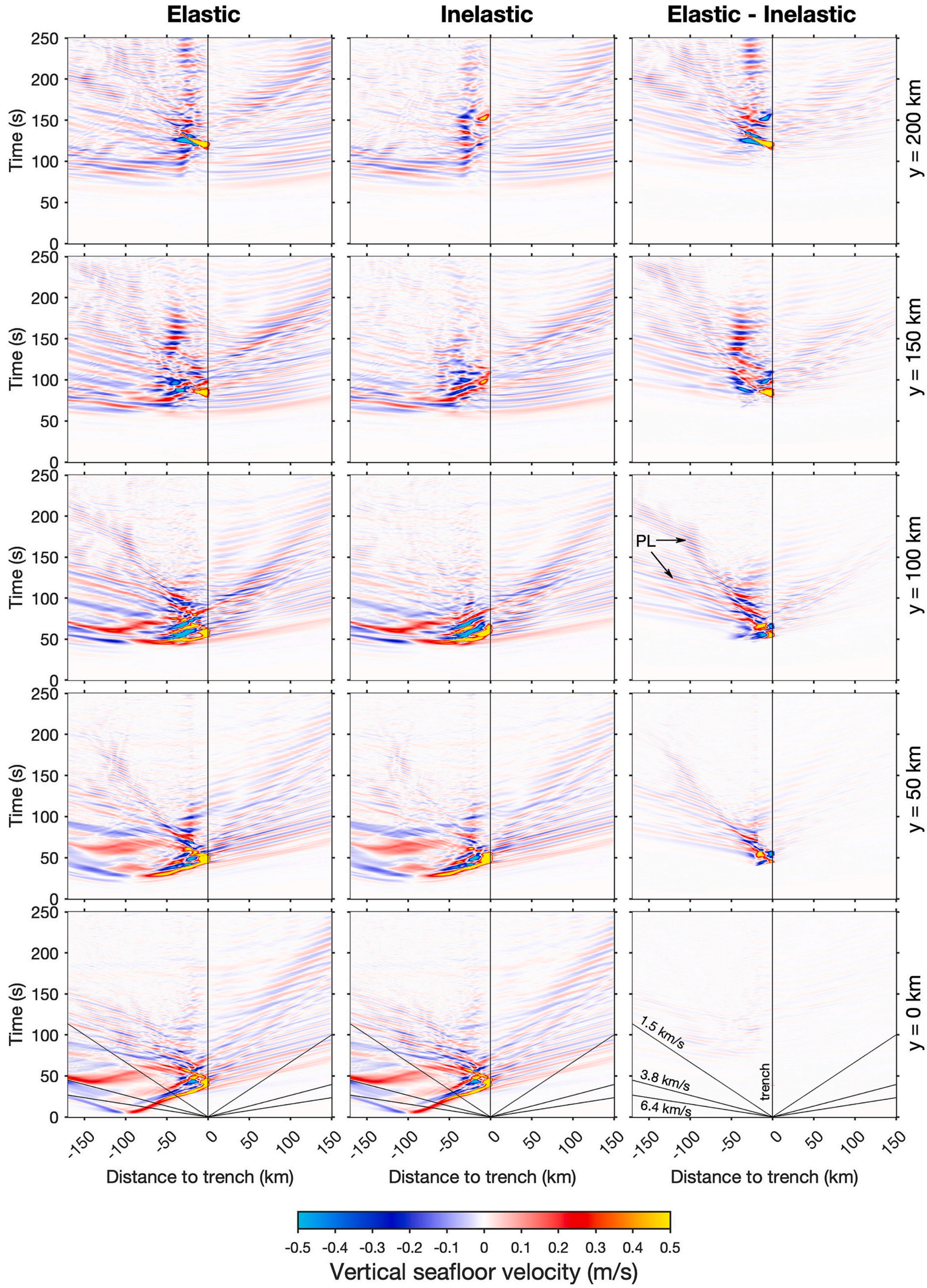

Fig. 8. Space-time plots of vertical seafloor velocity in elastic and inelastic models are illustrated at 5 cross sections. The difference between the two models is shown in the right column, depicting clearly stronger PL and oceanic Rayleigh waves radiated from rupture front and larger energy trapped within the sediment in the elastic model. (For interpretation of the references to colour in this figure legend, the reader is referred to the web version of this article.)

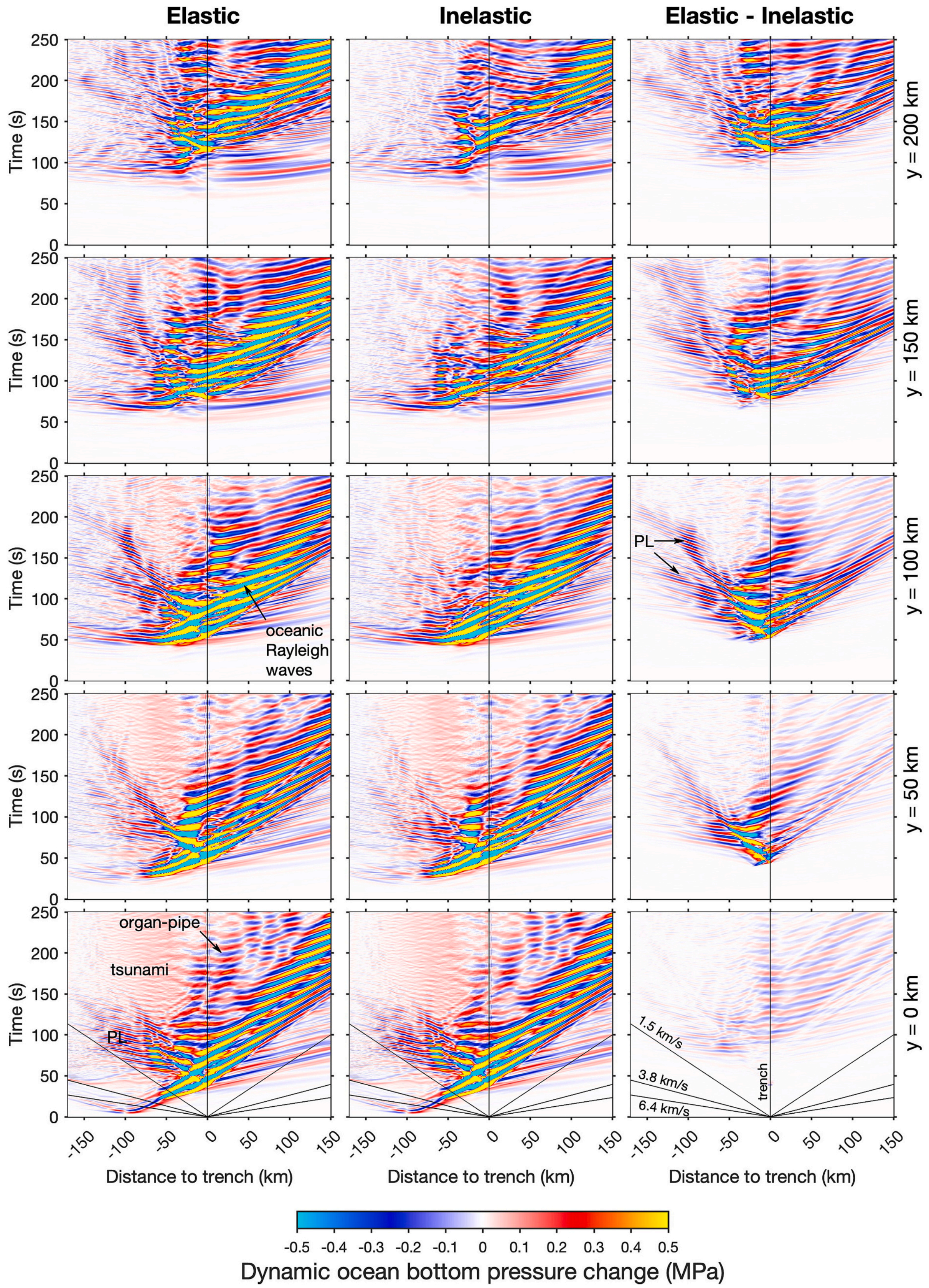

Fig. 9. Same as Fig. 8 except for dynamic ocean bottom pressure change. Larger organ-pipe waves in the elastic model can also be seen (marked in the lower left panel). The landward tsunami (in pink) is clearly seen in both models in the bottom three rows. (For interpretation of the references to colour in this figure legend, the reader is referred to the web version of this article.)

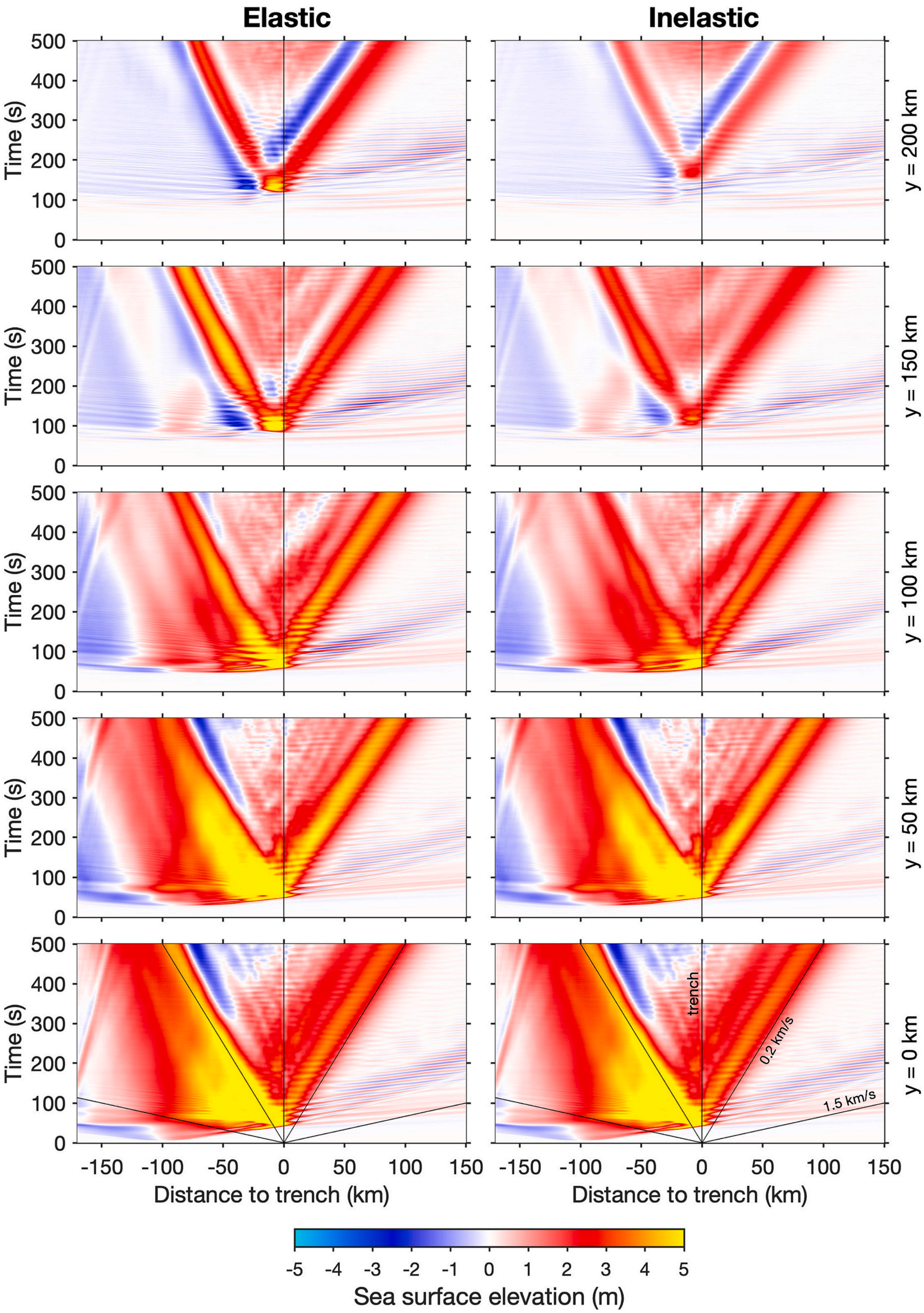

Fig. 10. Space-time plots of sea surface elevation for elastic and inelastic models are shown. Larger tsunami in the northern 3 cross sections in the elastic model due to larger slip at trench is seen, which, however, overpredicts the observations (Ma, 2023). Reflection from the coast is due to the artificial western ocean boundary in the models (Fig. 1). (For interpretation of the references to colour in this figure legend, the reader is referred to the web version of this article.)

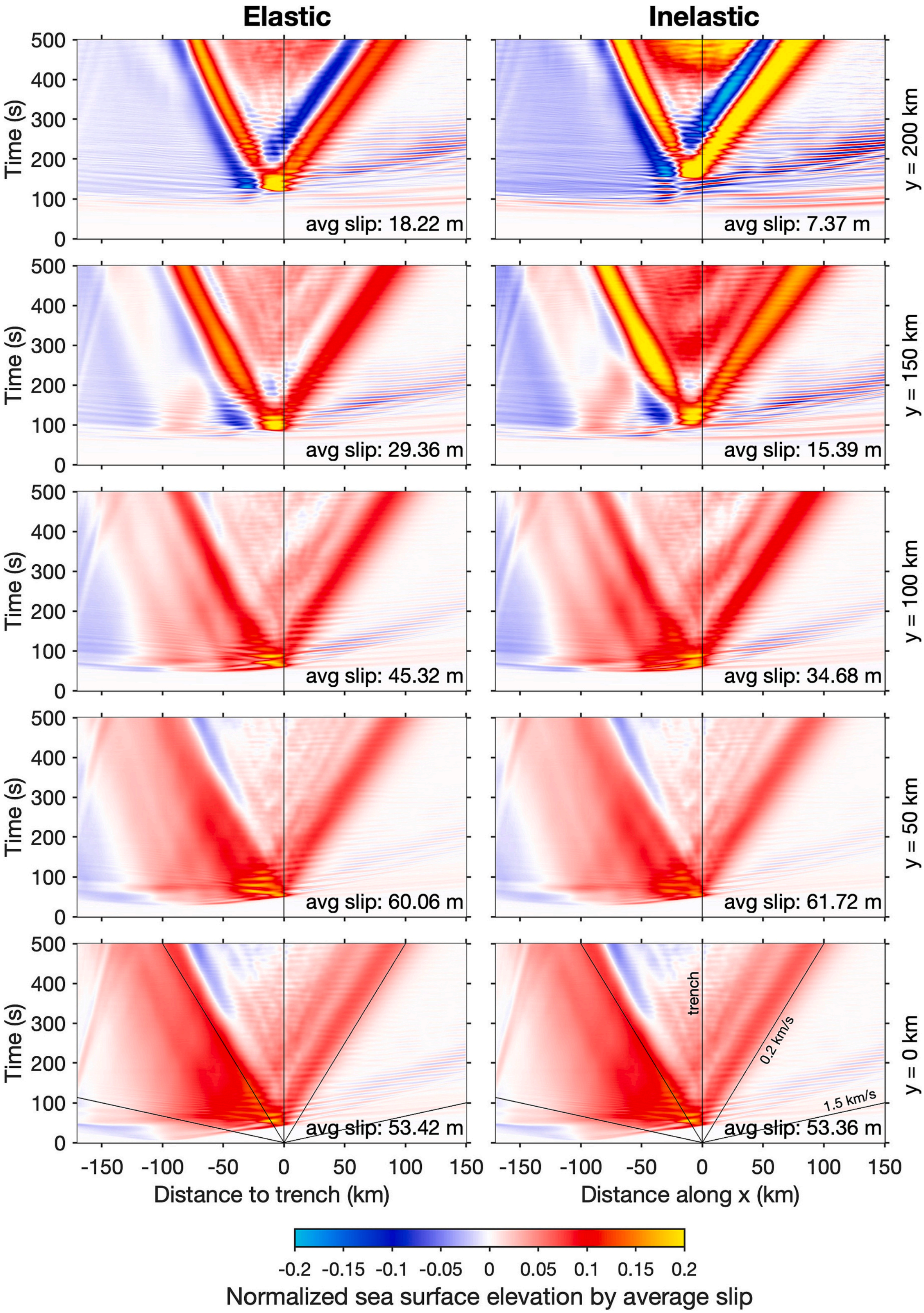

Fig. 11. Space-time plots of normalized sea surface elevation for elastic and inelastic models show higher efficiency in tsunami generation by inelastic wedge deformation in the northern Japan Trench. The efficiency is defined by the ratio of sea surface elevation to the average slip within 40 km from trench in each cross section (shown in the lower right corner of each panel). (For the interpretation of the references to colour in this figure legend, the reader is referred to the web version of this article.)

from the dynamic rupture model. At each time step, the contribution from horizontal displacement (Tanioka and Satake, 1996) is calculated and added to the seafloor uplift. Then, a lowpass Kajiura filter with a cutoff wavelength of 6 km (Kubota et al., 2022) was applied to filter out short-wavelength waves by the ocean (Kajiura, 1963) before entering it in the shallow water model. To account for tsunami dispersion, a Boussinesq equation needs to be solved. In the fully coupled model these effects have been considered in the sea surface and bottom boundary conditions. The agreement between the two models validates both approaches, especially when a constant cutoff wavelength was used in the shallow water model. Note that the ocean acoustic waves are clearly visible in the first 4 snapshots of Fig. 4a, but not in Fig. 4b. The slightly different tsunami amplitudes are largely due to the presence of ocean acoustic waves in the fully coupled model.

The slip distributions at $t = 500$ s for both the fully coupled elastic and inelastic models are shown in Figs. 5c and d. Rupture time contours every 10 s are depicted in black. They are very similar to the models of Ma (2023) without ocean, shown in Fig. 5a and b. The slip distributions and rupture velocities outside northern Japan Trench among all models are similar because of dominantly elastic off-fault response. North of 38.7°N, the large shallow slip and fast rupture velocity in the elastic models and diminishing shallow slip and slow rupture propagation in the inelastic models are clearly seen.

However, when we examine slip distributions more closely peak slip differs in a small patch near $y = 50$ km at the trench. The peak slip in the fully coupled model with inelastic deformation reaches 109.43 m, much larger than that in the fully coupled elastic model (85.17 m). In the two models without ocean, the peak slip in the inelastic model (75.67 m) is smaller than that of elastic model (87.63 m). The slip contours in blue also indicate that slip is slightly larger in the northern Japan Trench in the inelastic model with ocean than without ocean.

To find out what gives rise to such large slip in this small patch we show the space-time plots of the slip velocity along $y = 50$ km and relevant time histories at trench for all 4 models (Fig. 6). One feature to notice immediately is the longer slip duration near trench with inelastic deformation than elastic models (Fig. 6a – e). The peak slip rate is also reduced by inelastic deformation in models with or without ocean due to yielding and more gradual stress changes (Fig. 6e). In the two models without ocean the longer slip duration cannot compensate for the large reduction of peak slip rate so after time integration the final slip is still smaller in the inelastic model. We note a large reduction of peak slip rate in the elastic model with ocean compared to the model without ocean, which is likely due to the elasticity of ocean (compared to free surface) suppressing slip velocity during rupture breakout. In the inelastic model with ocean this reduction in peak slip rate is much smaller. However, there is a second peak in the slip rate, which coincides with the dilation caused by the reflected P waves from sea surface leading to normal stress reduction and additional stress drop on the fault. This strong dilation makes the slip rate with ocean larger than that without ocean for ~10 s, which gives rise to larger slip after time integration. In the elastic model with ocean this dilatational effect is also present. However, the large reduction of peak slip rate counteracts this effect, making the final slip with and without ocean about similar. Therefore, the combined effect of inelastic deformation and hydroacoustic dilation leads to long slip duration and large, localized slip in this small patch and slight increase in slip in the northern Japan Trench. This effect may only occur with modest inelastic deformation as the peak slip rates between elastic and inelastic models are similar. If intense inelastic deformation reduces slip rate significantly this combined effect cannot lead to large slip increase; instead diminished shallow slip should occur, as seen in the northern Japan Trench.

The horizontal and vertical surface displacements for the 2 models with ocean at 500 s are shown in Fig. 7. Although the peak horizontal and vertical displacements differ due to the difference in peak slip both models produce nearly identical fits to the GPS data, indicating limited resolution of GPS data to near-trench deformation. We point out that the large, localized slip patch is likely unimportant in tsunami generation because any features with wavelengths shorter than ocean depth are filtered out by the ocean (Kajiura, 1963), which can be seen in Fig. 4.

To better illustrate the differences in radiation characteristics between elastic and inelastic models we show the space-time plots of vertical seafloor velocity and dynamic ocean bottom pressure change, as well as the differences between elastic and inelastic models, along 5 cross sections in Figs. 8 and 9. At $y = 0$, the inelastic deformation is small, and there is little difference between the two models. Both models resemble closely the 2D dynamic rupture model for the 2011 Tohoku-Oki earthquake of Kozdon and Dunham (2014). The radiation from up- and down-dip rupture from hypocenter can be clearly seen. After rupture breakout at trench strong landward-propagating PL waves and seaward-propagating oceanic Rayleigh waves are strongly excited. There are also distinctly trapped *P* waves bouncing up and down (marked as organ pipe) in the models. The speed of PL waves exceeds the S-wave speeds of upper crustal layers in the JIVSM (see Fig. 2 of Ma, 2023), excluding the possibility of any surface waves and *S* waves. The landward tsunami is also clearly seen, which was not included in the model of Kozdon and Dunham (2014). As the rupture propagates northward, similar patterns are seen. PL and oceanic Rayleigh waves are generated at the trench with stronger radiation in the elastic model, which can be more clearly seen in the differences between the two models because common radiations from earlier ruptures are removed. The organ-pipe waves are also much stronger in the elastic model shown in Fig. 9. The differences between the two models increase to the north due to more significant inelastic deformation, causing weak radiation. The apparent velocity of PL wave seems larger as rupture propagates northward, which is due to the oblique incidence of these waves on the cross sections (Fig. 3). The trapped wave energy landward from trench appear to be the source of radiation as sediment thickens northward, with the effect being stronger in the elastic model. The slowest propagating PL wave trailing from behind the rupture front is seen to propagate with an apparent velocity less than 1.5 km/s, which is probably related to rupture velocity (see Fig. 3, Movies 1 and 2). The space-time plots of horizontal seafloor velocity are shown in Fig. S2, which shows similar results and indicates that particle motion is mostly in the same plane as the wave direction, confirming the identification of PL waves.

Fig. 10 shows the space-time plots of sea surface elevation. Clear tsunami propagation superimposed by ocean acoustic waves is seen. One feature to notice immediately is the longer-wavelength of tsunami at $y =$ 0 and 50 km caused by ~200 km rupture width. The width of rupture zone in the northern Japan Trench is only ~40 km, leading to impulsive tsunami as observed off Sanriku coast. Reduction of wavelength during shoaling is also clearly seen at $y = 0$ and 50 km. Tsunami amplitudes are nearly identical in the southern two cross sections between elastic and inelastic models because inelastic deformation is small. In the northern Japan Trench ($y = 150$ and 200 km), the tsunami amplitudes are larger in the elastic model due to >40 m shallow slip peaking at trench, which is inconsistent with the differential bathymetry observations. The elastic model also overestimates the tsunami amplitudes (Ma, 2023). If we normalize sea surface elevation by average slip within 40 km from trench at each section and define it as the efficiency of tsunami generation, we see that the efficiency is the largest in the two northern cross sections in the inelastic model (Fig. 11). We choose 40 km because it is about the width of rupture in the northern Japan Trench and the value used in the differential bathymetry studies to infer coseismic displacement near trench, which is also the major tsunami generation zone. The average slip at each cross section is shown in the lower right corner of each panel. The larger efficiency in the inelastic model is not surprising because inelastic deformation represents frictional sliding on microfractures with steeper dips than that of the plate interface. The inelastic model produces tsunami with diminishing shallow slip, consistent with the differential bathymetry observations, and match the amplitude and timing of tsunami observed off the Sanriku coast (Ma, 2023).

We show time histories of two components of seafloor velocity,

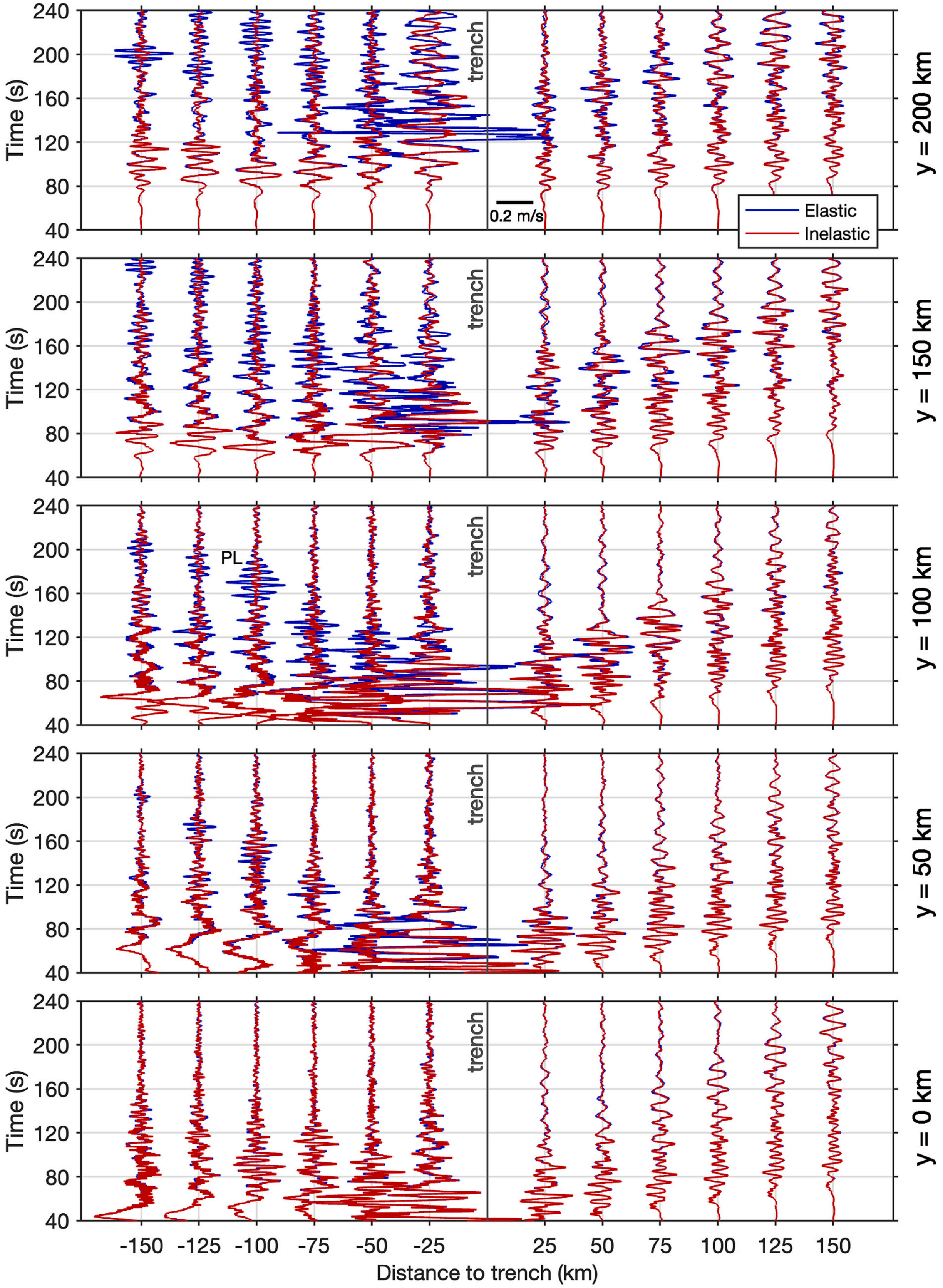

Fig. 12. Vertical seafloor velocity time histories are compared between elastic and inelastic models, showing stronger radiation landward from trench in the elastic model. (For the interpretation of the references to colour in this figure legend, the reader is referred to the web version of this article.)

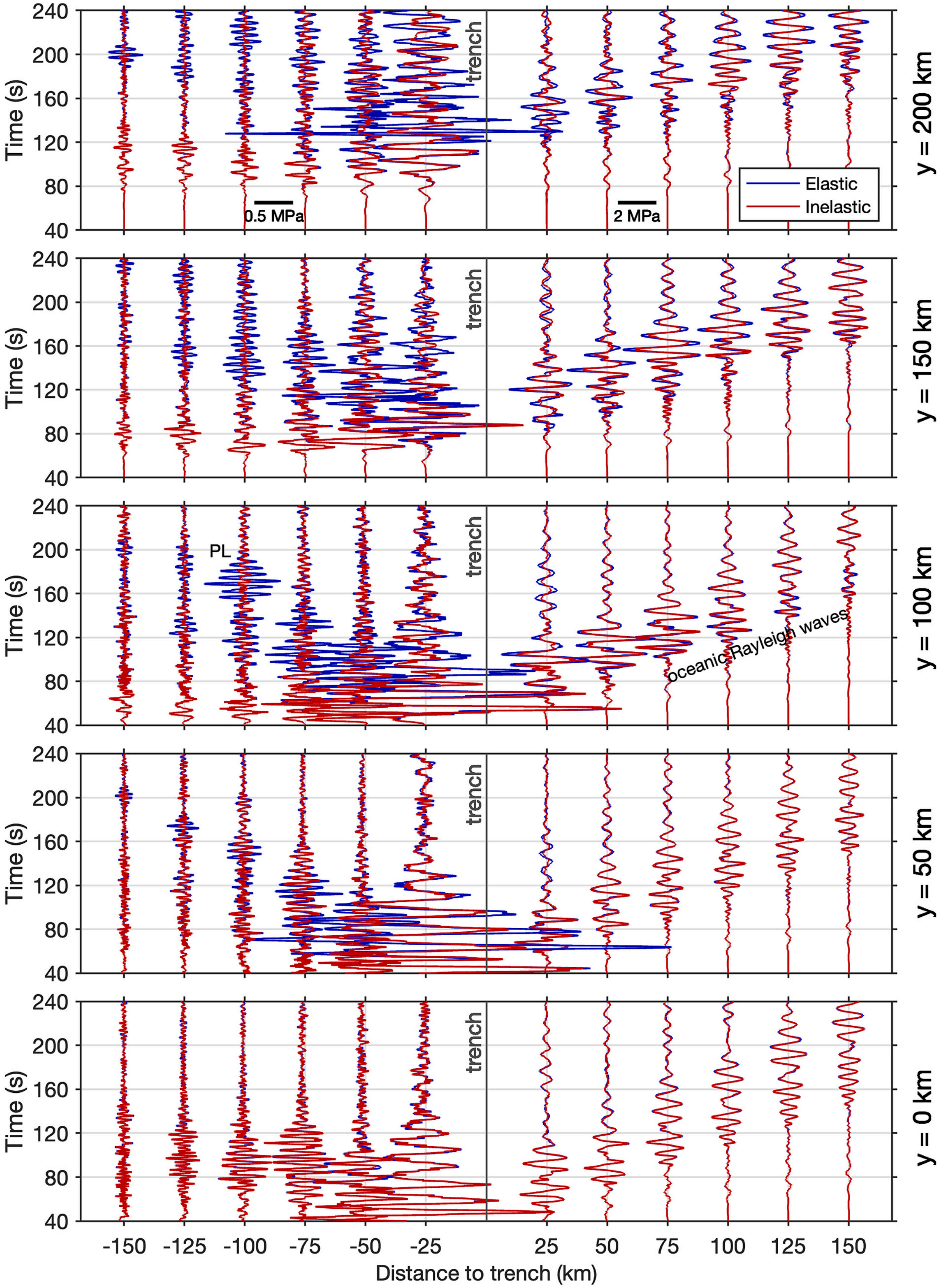

Fig. 13. Same as Fig. 12 except for dynamic ocean bottom pressure change. Different amplitude scales are used for landward and seaward from trench. (For interpretation of the references to colour in this figure legend, the reader is referred to the web version of this article.)

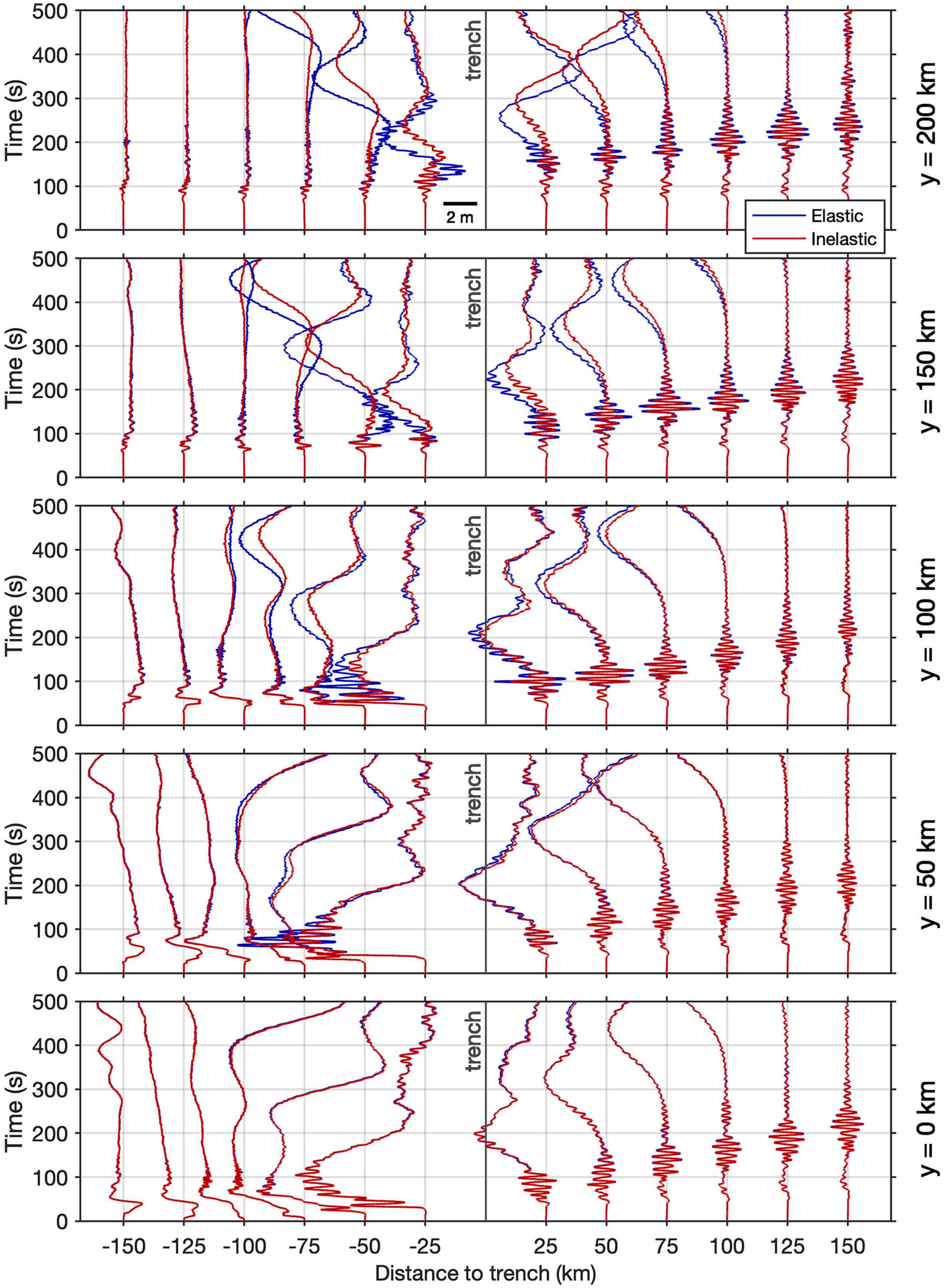

Fig. 14. Time-histories of sea surface elevation are compared between elastic and inelastic models. Note the different periods of ocean acoustic waves and tsunami. Larger tsunami in the northern Japan Trench in the elastic model overpredicts the tsunami observations (Ma, 2023). The higher efficiency of tsunami generation in the inelastic model is shown in Fig. 11. (For interpretation of the references to colour in this figure legend, the reader is referred to the web version of this article.)

dynamic ocean bottom pressure change, and sea surface elevation for the two models in Figs. 12–14 and S3. Again, the main difference between the two models is the radiation of ocean acoustic waves, mostly PL, organ pipe, oceanic Rayleigh waves, and trapped waves in the sedimentary wedge. Note that different scales are used for the landward and seaward sides from the trench in Fig. 13 because the ocean bottom pressure change is much larger in seaward-propagating oceanic Rayleigh waves (see also Fig. 9). Different periods of ocean acoustic waves and tsunami are clearly shown in Fig. 14.

4. Discussion and conclusions

The concept of using ocean acoustic waves in tsunami early warning can be traced back to Ewing et al. (1950), who proposed using T waves for tsunami warning. Okal et al. (2003) pointed out that T waves primarily reflect high-frequency characteristics of the source rather than the low-frequency processes controlling tsunami generation, which are particularly weak in tsunami earthquakes and can severely underestimate tsunami hazards. Kozdon and Dunham (2014) and Lay et al. (2019) proposed using PL waves for rapid estimate of shallow slip to issue tsunami warnings because these waves travel much faster than tsunami. They assumed that slip occurs rapidly with strong rupture breakout at trench in an elastic framework, similar to the elastic model in this work. As Kozdon and Dunham (2014) pointed out, the PL wave excitation can be significantly weaker if rapid slip does not occur. As shown in our inelastic model, the radiation of PL and other acoustic waves are significantly reduced by inelastic deformation, but devasting tsunami can be generated with slow rupture propagation despite reduced shallow slip. Other similar works (e.g., Mei and Kadri, 2017; Gomez and Kadri, 2023) advocating ocean acoustic waves for tsunami early warning may also have overlooked the deficiency in high-frequency radiation associated with large tsunamigenesis. Because tsunami has much longer period any application of high-frequency acoustic and seismic waves in early warnings on robust tsunami amplitude may be a challenge.

The large shallow slip hypothesis for tsunami generation has been widely used in subduction zones worldwide. Although >50 m slip updip from the hypocenter in the 2011 Tohoku-Oki earthquake was confirmed by the differential bathymetry observation this hypothesis violates the differential bathymetry observation north of 39°N. Neither can it account for the turbidite observations and depletion in high-frequency radiation along the Sanriku coast north of 39°N. Sediment in an elastic setting does not always lead to depletion in high-frequency radiation, contradicting many previous studies (e.g., Polet and Kanamori, 2000; Sallarès and Ranero, 2019). Slip models by inverting seismic data failed to resolve the rupture in the northern Japan Trench, which can also be due to depletion in high-frequency radiation. The elastic dislocation theory and large shallow slip hypothesis may not be universally applicable in sediment-filled margins, such as northern Japan Trench, accretionary plate boundaries, and even in strike-slip tectonic settings (e.g., Ma, 2022). Future rupture models for large tsunamigenic earthquakes probably need to address depletion in high-frequency radiation and tsunami generation together, as they reveal and constrain the important physics of tsunami generation.

We have shown that inelastic wedge deformation can explain both large tsunamigenesis and depletion in high-frequency radiation in the northern Japan Trench in fully coupled models of dynamic rupture, ocean acoustic waves, and tsunami for the 2011 M_W 9.1 Tohoku-Oki earthquake. Due to presence of thick sediment in the northern Japan Trench inelastic deformation of sediment generates large seafloor uplift (~4 m) with shallow slip much smaller than required to obtain comparable tsunami amplitude in elastic dislocation models (<20 m), consistent with the differential bathymetry observations. Meanwhile, inelastic deformation is a large energy sink (Ma and Hirakawa, 2013), which leads to slow rupture propagation (~850 m/s) and weak acoustic and seismic radiations. This mechanism provides a self-consistent explanation to large tsunamigenesis, depletion in high-frequency radiation, and the mysterious >100 km offset between the large tsunami north of 39°N and major shallow slip zone up dip from the hypocenter.

Physics of tsunamigenesis is essential in tsunami hazard reduction worldwide, pertinent to important issues such as whether ocean acoustic waves can be used in tsunami early warning discussed in this paper. Future seafloor observations, such as networks of collocated seismic and ocean bottom pressure sensors (Aoi et al., 2020) and geodetic stations, can help test both the large shallow slip and inelastic deformation hypotheses even further.

Supplementary data to this article can be found online at https://doi.org/10.1016/j.tecto.2025.230831.

CRediT authorship contribution statement

Shuo Ma: Writing – review & editing, Visualization, Validation, Supervision, Software, Resources, Project administration, Methodology, Investigation, Funding acquisition, Formal analysis, Data curation, Conceptualization. **Yue Du:** Writing – original draft, Visualization, Validation, Software, Methodology, Investigation, Formal analysis, Data curation, Conceptualization.

Declaration of Competing Interest

The authors declare that they have no known competing financial interests or personal relationships that could have appeared to influence the work reported in this paper.

Acknowledgements

We are grateful to David Tappin and an anonymous reviewer for constructive comments and Tatsuya Kubota and Tatsuhiko Saito for helpful discussions. This work was supported by the National Science Foundation (award no. EAR-2244703).

Data availability

Data will be made available on request.

References

Abrahams, L.S., Krenz, L., Dunham, E.M., Gabriel, A.-A., Saito, T., 2023. Comparison of methods for coupled earthquake and tsunami modelling. Geophys. J. Int. 234 (1), 404–426. https://doi.org/10.1093/gji/ggad053.

Aoi, S., Asano, Y., Kunugi, T., Kimura, T., Uehira, K., Takahashi, N., Ueda, H., Shiomi, K., Matsumoto, T., Fujiwara, H., 2020. MOWLAS: NIED observation network for earthquake, tsunami and volcano. Earth Planet Space 72 (1). https://doi.org/10.1186/s40623-020-01250-x.

Bilek, S.L., Lay, T., 2002. Tsunami earthquakes possibly widespread manifestations of frictional conditional stability. Geophys. Res. Lett. 29 (14). https://doi.org/10.1029/2002gl015215.

Cheung, K.F., Lay, T., Sun, L., Yamazaki, Y., 2021. Tsunami size variability with rupture depth. Nat. Geosci. 15 (1), 33–36. https://doi.org/10.1038/s41561-021-00869-z.

Du, Y., Ma, S., Kubota, T., Saito, T., 2021. Impulsive tsunami and large runup along the Sanriku coast of Japan produced by an inelastic wedge deformation model. J. Geophys. Res. Solid Earth 126 (8). https://doi.org/10.1029/2021jb022098.

Duan, B., 2012. Dynamic rupture of the 2011 M_W 9.0 Tohoku-Oki earthquake: Roles of a possible Subducting Seamount. J. Geophys. Res. Solid Earth 117 (B5). https://doi.org/10.1029/2011jb009124.

Ewing, M., Tolstoy, I., Press, F., 1950. Proposed use of the T phase in tsunami warning systems. Bull. Seismol. Soc. Am. 40 (1), 53–58. https://doi.org/10.1785/bssa0400010053.

Fujiwara, T., 2021. Seafloor geodesy from repeated multibeam bathymetric surveys: Application to seafloor displacement caused by the 2011 Tohoku-Oki earthquake. Front. Earth Sci. 9. https://doi.org/10.3389/feart.2021.667666.

Fujiwara, T., Kodaira, S., No, T., Kaiho, Y., Takahashi, N., Kaneda, Y., 2011. The 2011 Tohoku-Oki earthquake: Displacement reaching the Trench Axis. Science 334 (6060), 1240. https://doi.org/10.1126/science.1211554.

Fujiwara, T., dos Santos Ferreira, C., Bachmann, A.K., Strasser, M., Wefer, G., Sun, T., Kanamatsu, T., Kodaira, S., 2017. Seafloor displacement after the 2011 tohoku-oki earthquake in the Northern Japan Trench examined by repeated bathymetric surveys. Geophys. Res. Lett. 44 (23). https://doi.org/10.1002/2017gl075839.

Gomez, B., Kadri, U., 2023. Numerical validation of an effective slender fault source solution for past tsunami scenarios. Phys. Fluids 35 (4). https://doi.org/10.1063/5.0144360.

Gusman, A.R., Tanioka, Y., Sakai, S., Tsushima, H., 2012. Source model of the Great 2011 Tohoku earthquake estimated from tsunami waveforms and crustal deformation data. Earth Planet. Sci. Lett. 341–344, 234–242. https://doi.org/10.1016/j.epsl.2012.06.006.

Harris, R.A., Day, S.M., 1997. Effects of a low-velocity zone on a dynamic rupture. Bull. Seismol. Soc. Am. 87 (5), 1267–1280. https://doi.org/10.1785/bssa0870051267.

Hill, E.M., Borrero, J.C., Huang, Z., Qiu, Q., Banerjee, P., Natawidjaja, D.H., Elosegui, P., Fritz, H.M., Suwargadi, B.W., Pranantyo, I.R., Li, L., Macpherson, K.A., Skanavis, V., Synolakis, C.E., Sieh, K., 2012. The 2010 M_W 7.8 Mentawai earthquake: very shallow source of a rare tsunami earthquake determined from tsunami field survey and near-field GPS data. J. Geophys. Res. Solid Earth 117 (B6). https://doi.org/10.1029/2012jb009159.

Iinuma, T., Hino, R., Kido, M., Inazu, D., Osada, Y., Ito, Y., Ohzono, M., Tsushima, H., Suzuki, S., Fujimoto, H., Miura, S., 2012. Coseismic slip distribution of the 2011 off the Pacific coast of Tohoku earthquake (M9.0) refined by means of seafloor geodetic data. J. Geophys. Res. Solid Earth 117 (B7). https://doi.org/10.1029/2012jb009186.

Ikehara, K., Usami, K., Kanamatsu, T., Arai, K., Yamaguchi, A., Fukuchi, R., 2018. Spatial variability in sediment lithology and sedi- mentary processes along the Japan Trench: use of deep-sea turbidite records to reconstruct past large earthquakes. Geol. Soc. Lond. Spec. Publ. 456 (1), 75–89. https://doi.org/10.1144/SP456.9.

Kajiura, K., 1963. Leading Wave of a Tsunami, 41. Bulletin of the Earthquake Research Institute, pp. 535–571.

Kanamori, H., 1972. Mechanism of tsunami earthquakes. Phys. Earth Planet. Inter. 6 (5), 346–359. https://doi.org/10.1016/0031-9201(72)90058-1.

Kanamori, H., Kikuchi, M., 1993. The 1992 Nicaragua earthquake: a slow tsunami earthquake associated with subducted sediments. Nature 361 (6414), 714–716. https://doi.org/10.1038/361714a0.

Kato, A., Igarashi, T., 2012. Regional extent of the large coseismic slip zone of the 2011 MW 9.0 tohoku-oki earthquake delineated by on-fault aftershocks. Geophys. Res. Lett. 39 (15). https://doi.org/10.1029/2012gl052220.

Kido, M., Osada, Y., Fujimoto, H., Hino, R., Ito, Y., 2011. Trench-normal variation in observed seafloor displacements associated with the 2011 Tohoku-Oki earthquake. Geophys. Res. Lett. 38 (24). https://doi.org/10.1029/2011gl050057.

Kodaira, S., Nakamura, Y., Yamamoto, Y., Obana, K., Fujie, G., No, T., Kaiho, Y., Sato, T., Miura, S., 2017. Depth-varying structural characters in the rupture zone of the 2011 Tohoku-Oki earthquake. Geosphere 13 (5), 1408–1424. https://doi.org/10.1130/ges01489.1.

Kodaira, S., Fujiwara, T., Fujie, G., Nakamura, Y., Kanamatsu, T., 2020. Large coseismic slip to the trench during the 2011 Tohoku-Oki earthquake. Annu. Rev. Earth Planet. Sci. 48 (1), 321–343. https://doi.org/10.1146/annurev-earth-071719-055216.

Kodaira, S., Iinuma, T., Imai, K., 2021. Investigating a tsunamigenic megathrust earthquake in the Japan Trench. Science 371 (6534). https://doi.org/10.1126/science.abe1169.

Koketsu, K., Miyake, H., Suzuki, H., 2012. Japan integrated velocity structure model version 1. In: Proceedings of the 15th world conference on earthquake engineering. https://www.iitk.ac.in/nicee/wcee/article/WCEE2012_1773.pdf.

Kozdon, J.E., Dunham, E.M., 2014. Constraining shallow slip and tsunami excitation in megathrust ruptures using seismic and ocean acoustic waves recorded on ocean-bottom sensor networks. Earth Planet. Sci. Lett. 396, 56–65. https://doi.org/10.1016/j.epsl.2014.04.001.

Kubota, T., Saito, T., Hino, R., 2022. A new mechanical perspective on a shallow megathrust near-trench slip from the high-resolution fault model of the 2011 Tohoku-Oki earthquake. Progr. Earth Planet. Sci. 9 (1). https://doi.org/10.1186/s40645-022-00524-0.

Kurahashi, S., Irikura, K., 2013. Short-period source model of the 2011 M_W 9.0 off the pacific coast of Tohoku earthquake. Bull. Seismol. Soc. Am. 103 (2B), 1373–1393. https://doi.org/10.1785/0120120157.

Kutschera, F., Gabriel, A.-A., Wirp, S.A., Li, B., Ulrich, T., Abril, C., Halldórsson, B., 2024. Linked and fully coupled 3D earthquake dynamic rupture and tsunami modeling for the Húsavík–Flatey Fault Zone in North Iceland. Solid Earth 15, 251–280. https://doi.org/10.5194/se-15-251-2024.

Lay, T., 2018. A review of the rupture characteristics of the 2011 Tohoku-Oki MW 9.1 earthquake. Tectonophysics 733, 4–36. https://doi.org/10.1016/j.tecto.2017.09.022.

Lay, T., Kanamori, H., Ammon, C.J., Koper, K.D., Hutko, A.R., Ye, L., Yue, H., Rushing, T. M., 2012. Depth-varying rupture properties of subduction zone megathrust faults. J. Geophys. Res. Solid Earth 117 (B4). https://doi.org/10.1029/2011jb009133.

Lay, T., Liu, C., Kanamori, H., 2019. Enhancing tsunami warning using P wave coda. J. Geophys. Res. Solid Earth 124, 10,583–10,609. https://doi.org/10.1029/2019JB018221.

Lotto, G.C., Dunham, E.M., 2015. High-order finite difference modeling of tsunami generation in a compressible ocean from offshore earthquakes. Comput. Geosci. 19 (2), 327–340. https://doi.org/10.1007/s10596-015-9472-0.

Lotto, G.C., Dunham, E.M., Jeppson, T.N., Tobin, H.J., 2017. The effect of compliant prisms on subduction zone earthquakes and Tsunamis. Earth Planet. Sci. Lett. 458, 213–222. https://doi.org/10.1016/j.epsl.2016.10.050.

Lotto, G.C., Jeppson, T.N., Dunham, E.M., 2018. Fully coupled simulations of megathrust earthquakes and tsunamis in the Japan Trench, Nankai Trough, and Cascadia subduction zone. Pure Appl. Geophys. 176 (9), 4009–4041. https://doi.org/10.1007/s00024-018-1990-y.

Ma, K., Brodsky, E.E., Mori, J., Ji, C., Song, T.A., Kanamori, H., 2003. Evidence for fault lubrication during the 1999 Chi-Chi, Taiwan, earthquake (M_W7.6). Geophys. Res. Lett. 30 (5). https://doi.org/10.1029/2002gl015380.

Ma, S., 2008. A physical model for widespread near-surface and fault zone damage induced by earthquakes. Geochem. Geophys. Geosyst. 9 (11). https://doi.org/10.1029/2008gc002231.

Ma, S., 2012. A self-consistent mechanism for slow dynamic deformation and tsunami generation for earthquakes in the shallow subduction zone. Geophys. Res. Lett. 39 (11). https://doi.org/10.1029/2012gl051854.

Ma, S., 2022. Dynamic off-fault failure and tsunamigenesis at strike-slip restraining bends: Fully-coupled models of dynamic rupture, ocean acoustic waves, and tsunami in a shallow bay. Tectonophysics 838, 229496. https://doi.org/10.1016/j.tecto.2022.229496.

Ma, S., 2023. Wedge plasticity and a minimalist dynamic rupture model for the 2011 M_W 9.1 Tohoku-Oki earthquake and tsunami. Tectonophysics 869, 230146. https://doi.org/10.1016/j.tecto.2023.230146.

Ma, S., Andrews, D.J., 2010. Inelastic off-fault response and three-dimensional dynamics of earthquake rupture on a strike-slip fault. J. Geophys. Res. Solid Earth 115 (B4). https://doi.org/10.1029/2009jb006382.

Ma, S., Beroza, G.C., 2008. Rupture dynamics on a bimaterial interface for dipping faults. Bull. Seismol. Soc. Am. 98 (4), 1642–1658. https://doi.org/10.1785/0120070201.

Ma, S., Hirakawa, E.T., 2013. Dynamic wedge failure reveals anomalous energy radiation of shallow subduction earthquakes. Earth Planet. Sci. Lett. 375, 113–122. https://doi.org/10.1016/j.epsl.2013.05.016.

Ma, S., Nie, S., 2019. Dynamic wedge failure and along-arc variations of tsunamigenesis in the Japan Trench margin. Geophys. Res. Lett. 46 (15), 8782–8790. https://doi.org/10.1029/2019gl083148.

MacInnes, B.T., Gusman, A.R., LeVeque, R.J., Tanioka, Y., 2013. Comparison of earthquake source models for the 2011 Tohoku event using tsunami simulations and near-field observations. Bull. Seismol. Soc. Am. 103 (2B), 1256–1274. https://doi.org/10.1785/0120120121.

Maeda, T., Furumura, T., Sakai, S., Shinohara, M., 2011. Significant tsunami observed at ocean-bottom pressure gauges during the 2011 off the Pacific coast of Tohoku earthquake. Earth Planet Space 63 (7), 803–808. https://doi.org/10.5047/eps.2011.06.005.

Mei, C.C., Kadri, U., 2017. Sound signals of tsunamis from a slender fault. J. Fluid Mech. 836, 352–373. https://doi.org/10.1017/jfm.2017.811.

Meng, Q., Duan, B., 2023. Do upper-plate material properties or fault frictional properties play more important roles in tsunami earthquake characteristics? Tectonophysics 850, 229765. https://doi.org/10.1016/j.tecto.2023.229765.

Mori, N., Takahashi, T., Yasuda, T., Yanagisawa, H., 2011. Survey of 2011 Tohoku earthquake tsunami inundation and run-up. Geophys. Res. Lett. 38 (7). https://doi.org/10.1029/2011gl049210.

Newman, A.V., Okal, E.A., 1998. Teleseismic estimates of radiated seismic energy: the *E*/*m*0 discriminant for tsunami earthquakes. J. Geophys. Res. Solid Earth 103 (B11), 26885–26898. https://doi.org/10.1029/98jb02236.

Noda, H., Lapusta, N., 2013. Stable creeping fault segments can become destructive as a result of dynamic weakening. Nature 493 (7433), 518–521. https://doi.org/10.1038/nature11703.

Okal, E.A., 1988. Seismic parameters controlling far-field tsunami amplitudes: a Review. Nat. Hazards 1 (1), 67–96. https://doi.org/10.1007/bf00168222.

Okal, E.A., Alasset, P.-J., Hyvernaud, O., Schindelé, F., 2003. The deficient *t* waves of tsunami earthquakes. Geophys. J. Int. 152 (2), 416–432. https://doi.org/10.1046/j.1365-246x.2003.01853.x.

Oliver, J., Major, M., 1959. Leaking modes and the PL phase. Seismol. Res. Lett. 30 (2), 18. https://doi.org/10.1785/gssrl.30.2.18a.

Phinney, R.A., 1961. Leaking modes in the crustal waveguide: 1. The oceanic *pl* wave. J. Geophys. Res. 66 (5), 1445–1469. https://doi.org/10.1029/jz066i005p01445.

Polet, J., Kanamori, H., 2000. Shallow subduction zone earthquakes and their tsunamigenic potential. Geophys. J. Int. 142 (3), 684–702. https://doi.org/10.1046/j.1365-246x.2000.00205.x.

Sallarès, V., Ranero, C.R., 2019. Upper-plate rigidity determines depth-varying rupture behaviour of megathrust earthquakes. Nature 576 (7785), 96–101. https://doi.org/10.1038/s41586-019-1784-0.

Satake, K., Tanioka, Y., 1999. Sources of tsunami and tsunamigenic earthquakes in subduction zones. In: Seismogenic and Tsunamigenic Processes in Shallow Subduction Zones, 467–483. https://doi.org/10.1007/978-3-0348-8679-6_5.

Satake, K., Fujii, Y., Harada, T., Namegaya, Y., 2013. Time and space distribution of coseismic slip of the 2011 Tohoku earthquake as inferred from tsunami waveform data. Bull. Seismol. Soc. Am. 103 (2B), 1473–1492. https://doi.org/10.1785/0120120122.

Sato, M., Ishikawa, T., Ujihara, N., Yoshida, S., Fujita, M., Mochizuki, M., Asada, A., 2011. Displacement above the hypocenter of the 2011 Tohoku-Oki earthquake. Science 332 (6036), 1395. https://doi.org/10.1126/science.1207401.

Scholz, C.H., 2014. The rupture mode of the shallow large-slip surge of the Tohoku-Oki earthquake. Bull. Seismol. Soc. Am. 104 (5), 2627–2631. https://doi.org/10.1785/0120140130.

Seno, T., 2000. The 21 September, 1999 Chi-Chi earthquake in Taiwan: Implications for tsunami earthquakes. Terr. Atmos. Ocean. Sci. 11 (3), 701. https://doi.org/10.3319/tao.2000.11.3.701(cce).

Shimozono, T., Cui, H., Pietrzak, J.D., Fritz, H.M., Okayasu, A., Hooper, A.J., 2014. Short wave amplification and extreme runup by the 2011 Tohoku tsunami. Pure Appl. Geophys. 171 (12), 3217–3228. https://doi.org/10.1007/s00024-014-0803-1.

Sun, T., Wang, K., Fujiwara, T., Kodaira, S., He, J., 2017. Large fault slip peaking at trench in the 2011 Tohoku-Oki earthquake. Nat. Commun. 8 (1). https://doi.org/10.1038/ncomms14044.

Tanioka, Y., Satake, K., 1996. Tsunami generation by horizontal displacement of Ocean Bottom. Geophys. Res. Lett. 23 (8), 861–864. https://doi.org/10.1029/96gl00736.

Tanioka, Y., Seno, T., 2001a. Detailed analysis of tsunami waveforms generated by the 1946 Aleutian tsunami earthquake. Nat. Hazards Earth Syst. Sci. 1 (4), 171–175. https://doi.org/10.5194/nhess-1-171-2001.

Tanioka, Y., Seno, T., 2001b. Sediment effect on tsunami generation of the 1896 Sanriku tsunami earthquake. Geophys. Res. Lett. 28 (17), 3389–3392. https://doi.org/10.1029/2001gl013149.

Tappin, D.R., Grilli, S.T., Harris, J.C., Geller, R.J., Masterlark, T., Kirby, J.T., Shi, F., Ma, G., Thingbaijam, K.K.S., Mai, P.M., 2014. Did a submarine landslide contribute to the 2011 Tohoku tsunami? Mar. Geol. 357, 344–361. https://doi.org/10.1016/j.margeo.2014.09.043.

Tsuru, T., Park, J., Miura, S., Kodaira, S., Kido, Y., Hayashi, T., 2002. Along-arc structural variation of the plate boundary at the Japan Trench margin: Implication of interplate coupling. J. Geophys. Res. Solid Earth 107 (B12). https://doi.org/10.1029/2001jb001664.

Uchida, N., Bürgmann, R., 2021. A decade of lessons learned from the 2011 Tohoku-Oki earthquake. Rev. Geophys. 59 (2). https://doi.org/10.1029/2020rg000713.

Ueda, H., Kitazato, H., Jamieson, A., Bond, T., Cardigos, S., Funaki, M., Maroni, P.J., Nanbu, H., O'Callaghan, J.M., Onishi, T., Pedersen, S.W., Roperez, J., Tsuruzono, H., Watanabe, H.K., Yasuda, T., 2023. The submarine fault scarp of the 2011 Tohoku-Oki earthquake in the Japan Trench. Commun. Earth Environ. 4 (1). https://doi.org/10.1038/s43247-023-01118-4.

Wilson, A., Ma, S., 2021. Wedge plasticity and fully coupled simulations of dynamic rupture and tsunami in the Cascadia subduction zone. J. Geophys. Res. Solid Earth 126 (7). https://doi.org/10.1029/2020jb021627.

Yamazaki, Y., Cheung, K.F., Lay, T., 2018. A self-consistent fault slip model for the 2011 Tohoku earthquake and Tsunami. J. Geophys. Res. Solid Earth 123 (2), 1435–1458. https://doi.org/10.1002/2017jb014749.

Yao, H., Shearer, P.M., Gerstoft, P., 2013. Compressive sensing of frequency-dependent seismic radiation from subduction zone megathrust ruptures. Proc. Natl. Acad. Sci. 110 (12), 4512–4517. https://doi.org/10.1073/pnas.1212790110.

Ye, L., Lay, T., Kanamori, H., Rivera, L., 2016. Rupture characteristics of major and great ($mw \geq 7.0$) megathrust earthquakes from 1990 to 2015: 2. Depth dependence. J. Geophys. Res. Solid Earth 121 (2), 845–863. https://doi.org/10.1002/2015jb012427.

Yin, J., Denolle, M., 2021. The Earth surface controls the depth-dependent seismic radiation of megathrust earthquakes. AGU Adv. https://doi.org/10.1002/essoar.10506212.1.

Zhang, K., Wang, Y., Luo, Y., Zhao, D., Wang, M., Yang, F., Wu, Z., 2023. Complex tsunamigenic near-trench seafloor deformation during the 2011 Tohoku–Oki Earthquake. Nat. Commun. 14 (1). https://doi.org/10.1038/s41467-023-38970-z.